# Reynolds Number Dependence of Unbounded Stratified Shear Turbulence: A New Framework for Comparing Ocean and Laboratory Scale Measurements

Daniel G. MacDonald

Department of Civil and Environmental Engineering, University of Massachusetts Dartmouth
Department of Estuarine and Ocean Sciences, University of Massachusetts Dartmouth

**For Submittal to the *Journal of Geophysical Research - Oceans***

Corresponding author information:

Daniel G. MacDonald
Department of Civil and Environmental Engineering
University of Massachusetts Dartmouth
285 Old Westport Road
Dartmouth, MA 02747

Email: dmacdonald @umassd.edu
Phone: 508-910-6334

**Three Key Points of Research:**

1. The vertical scale (thickness) of the stratified shear layer plays a key role in setting the magnitude of the turbulent velocity scale.
2. Turbulence can be sustained at high bulk Richardson numbers when a layer Reynolds number is high.
3. Turbulence is amplified for small Reynolds numbers when turbulent instabilities are comparable in scale to shear layer thickness.

**Plain Language Summary:**

Many important processes in the ocean are strongly influenced by mixing, which helps to move material throughout the ocean and can also act like friction by slowing down the movement of ocean water. Mixing is the result of turbulence, a random or chaotic motion, which is in turn the result of changes in water speed below the surface. This study focuses on a specific type of ocean turbulence known as stratified-shear turbulence. Most attempts to predict the intensity of this kind of mixing rely only on changes in water speed and related changes in temperature or salinity. The thickness of the layer, where these changes occur, which can range from a few centimeters to 100s of meters, has rarely been taken into account. By comparing laboratory and ocean measurements, this study identifies, for the first time, that this layer thickness may play a crucial role in accurately predicting mixing. Surprisingly, thicker ocean layers result in relatively less intense mixing than thinner laboratory layers. Laboratory and computer simulations are often used to help us learn and make predictions about the ocean and the atmosphere; all of which could be substantially improved with this new insight.

## Abstract

Advances in understanding of stratified-shear turbulence have been made over the last several decades through ocean measurements, which typically quantify net turbulent quantities, and through laboratory and direct numerical simulations (DNS), which have sufficient resolution to investigate the internal dynamics of individual instabilities. Stratified shear layer thicknesses in these environments can range from cms for laboratory and DNS studies to 100s of m in ocean environments, complicating extrapolation of results between environments. This study provides a direct comparison of field measurements from oceanic stratified shear environments with laboratory flows, demonstrating that non-dimensional turbulent quantities at ocean scales can fall several orders of magnitude below laboratory values for similar bulk Richardson numbers, $\boldsymbol{Ri_B}$, suggesting that scale plays a critical role. Here, the dependence of the non-dimensional turbulence intensity, expressed as $\hat{a} = \frac{u_*}{\Delta u}$, on a layer Reynolds number, $\boldsymbol{Re}$, is evaluated via a ratio of the shear layer thickness, $h$, to the Kolmogorov turbulence length scale, $\eta$. Using a mechanistically driven, empirical approach a parameterization for turbulence is defined in $\boldsymbol{Ri_B}$ – $\frac{h}{\eta}$ parameter space, and by extension, $\boldsymbol{Ri_B}$ - $\boldsymbol{Re}$ parameter space. The mechanisms invoke a "building block" approach to initiation of stratified shear turbulence, which explains the presence of turbulence $\boldsymbol{Ri_B}$ values exceeding the critical value of the gradient Richardson number, $\boldsymbol{Ri_g}$, and increases in $\hat{a}$ at low $\boldsymbol{Re}$. The results describe a new "turbulent geography" in the $\boldsymbol{Ri_B}$ – $\boldsymbol{Re}$ plane that can build intuition about stratified shear turbulence and facilitate interpretation of ocean measurements in comparison to laboratory experiments and modeling.

## 1. Stratified Shear Turbulence

Stratified-shear layers occur in nature across a wide range of vertical scales. Laboratory experiments (e.g. Ellison and Turner 1959; Yuan and Horner-Devine 2013) are often performed with stratified-shear layers centimeters thick, while salt marsh – tidal flat exchange (e.g. Carr et al 2018) can form stratified shear layers tens of cm thick, and many estuarine and river plume stratified-shear layers (e.g., MacDonald et al 2007; Kilcher et al 2012) are on the order of meters. Deep ocean flows, such as the Mediterranean outflow (e.g., Barringer and Price 1997) or Faroes Bank overflow (Fer et al 2010), can create stratified-shear layers 100s of meters or more in thickness. Despite their vast differences in thickness, these flows tend to generate turbulence that is qualitatively, and often quantitatively, similar in terms of structure, and the differences in scale are often overlooked. Localized ratios of density and velocity gradients, in the form of a Richardson number, are typically utilized to describe the generation and intensity of stratified-shear turbulence, while the overall layer thickness is assumed of secondary importance, at best.

In practice, measurements of turbulence in the ocean necessarily represent averages of turbulent quantities across some spatial and/or temporal domain, as even modern measurement techniques are incapable of isolating and resolving the evolution of individual turbulent events (e.g., Kelvin-Helmholz billows). This is sufficient for most oceanographic applications where understanding large scale water mass modification and/or energy dissipation is typically the goal. In contrast, laboratory experiments and direct numerical simulation (DNS) can analyze individual turbulent events, but only for shear layer thicknesses much smaller than ocean scales (e.g. Shih et al 2000; Smyth et al 2001; Mashayek et al 2017a). Although significant advances in understanding turbulence have been made through both observational and laboratory/DNS studies, efforts to synthesize these differing views of turbulence are sometimes problematic. An example is that of mixing efficiency, where recent advances in DNS have allowed predictions of mixing efficiencies that greatly exceed the canonical value of 0.2 during certain phases of the life cycle of a Kelvin-Helmholz billow (e.g., Sahelipour and Peltier 2019). However, estimates of mixing efficiencies derived from observational data (e.g., Gregg et al 2018) necessarily tend toward an average (or "effective") value, consistent with the canonical value of 0.2. Without a framework for understanding field observations of turbulence comparatively with their smaller scale laboratory and DNS counterparts, relating these approaches will continue to be a challenging endeavour, compromising the use of DNS and laboratory experiments to inform understanding of turbulence at oceanic or atmospheric scales (e.g. Mashayek and Peltier, 2011; Odier et al 2009).

In this study, we seek an effective mechanism for explaining observed differences between ocean scale and laboratory/DNS scale turbulence, and propose a mechanistically based empirical framework for predicting turbulent quantities as a function of both the Richardson number and a layer Reynolds number, which encapsulates the effect of scale. The focus of the effort is on the net effect of turbulent activity, rather than the internal dynamics of individual turbulent events and may prove most valuable in the interpretation of field scale measurements and their relation to laboratory/DNS studies.

### 1.1 Length and velocity scales

Turbulence in unbounded stratified-shear environments is characterized by the presence of gradients in both density and velocity, generating competing influences towards stability and instability, respectively. This imbalance is typically characterized by a gradient Richardson number:

$$Ri_g = -\frac{g}{\rho_o}\frac{\partial \rho}{\partial z}\left(\frac{\partial u}{\partial z}\right)^{-2} \quad (1)$$

where $g$ represents gravitational acceleration, ρ is density (with $\rho_o$ a representative value), and $u$ represents the horizontal velocity. Note that $u$ and ρ in (1) are intended to be instantaneous, highly resolved representations of the local velocity and density fields. As noted by Miles (1961) and Howard (1961), a value of $\boldsymbol{Ri_g}$ less than or equal to 0.25 is a necessary condition for the generation of instabilities and turbulence. Turbulence in stratified shear environments can be initiated by the development of vortices, such as Kelvin-Helmholtz billows (Thorpe 1969), or Holmboe instabilities (e.g., Smyth and Peltier 1989; Lawrence et al 2013, Salehipour et al 2016a), which subsequently decay to turbulence, as shown in figure 1. Here, the fluids at the top and bottom are of constant velocity and density, and are separated by the stratified-shear layer, of order $h$ in vertical extent. The entire flow structure is distant from any boundaries which could impose a boundary layer across the region. In many ocean environments the extent of the shear and density gradient layers do not exactly overlap. In these cases, an approximation of $h$ can be generated considering the flux of density anomalies relative to each layer.

The outer, or overturning, scale of the Kelvin-Helmholtz process (e.g., figure 1) is related to the Ozmidov scale (e.g. Gregg 1987), $L_O = (\varepsilon N^{-3})^{\frac{1}{2}}$, where ε represents the dissipation rate of turbulent kinetic energy (TKE) and $N = [-(g/\rho_o)(\partial\rho/\partial z)]^{\frac{1}{2}}$ is the buoyancy frequency. The ratio of the overturning scale to the Ozmidov scale is a function of the turbulence age (e.g. Smyth et al 2001), but is typically of order one (Ferron et al 1998, MacDonald et al 2013), particularly in the aggregate for stratified shear turbulence. Although Geyer et al (2010) observed overturn-like structures at scales an order of magnitude or more larger than the

Ozmidov scale in estuarine stratified shear flows using acoustic techniques, actual mixing processes in that study appeared to be associated with the order $L_o$ overturns embedded in the braids of the larger structure. At the other end of the turbulent spectra, the smallest scales are constrained by the transfer of TKE to heat by the fluid viscosity, and characterized by the Kolmogorov scale, $\eta = (\nu^3 \epsilon^{-1})^{\frac{1}{4}}$, where $\nu$ is the kinematic viscosity. Similar dissipative processes for scalars (e.g., heat and/or salinity) occur at the related Bachelor scales. For ocean turbulence, $L_O \gg \eta$, and both scales may be fundamentally different than the shear layer thickness, $h$, as illustrated in figure 1.

Similarly, key velocity scales can be defined, including (1) the bulk velocity scale, $\Delta u$, which represents the velocity difference between the upper and lower layers, (2) the turbulent velocity scale, $u'$, representative of the outer scale turbulent velocity, and here assumed equivalent to the turbulent shear velocity (i.e., $u' \sim u_* = \left(\frac{\tau}{\rho}\right)^{\frac{1}{2}}$, where $\tau$ represents a turbulent interfacial stress), and (3) an entrainment velocity, $w_e$, which represents the one-way entrainment of fluid across isopycnals (e.g., MacDonald and Geyer 2004). In many cases, researchers have assumed that the entrainment velocity scales with the turbulent velocity such that $u' \sim w_e$ (e.g. Wells et al 2010; Strang and Fernando 2001), as entrainment and turbulence are related processes. However, the entrainment process represents one-way transport of fluid across the shear layer, while the turbulent velocity scale represents a balanced exchange of fluid (MacDonald and Geyer 2004), and thus, these two parameters may differ substantially, as expressed by their ratio, $a_* = \frac{u_*}{w_e}$ (Christodoulo 1986). Likewise, we define a second velocity scale ratio

$$\hat{a} = \frac{u_*}{\Delta u} \qquad (2A)$$

which represents the ratio of the turbulent to bulk velocity scales, and can be particularly useful for interpretation of field observations. Note that $\hat{a}^2$ is functionally equivalent to an interfacial drag coefficient, $C_{Di}$, and also to a non-dimensional form of the eddy viscosity, $\frac{\upsilon_T}{h\Delta u}$.

In our effort to parameterize turbulence as a function of bulk scale variables (e.g., those easily obtained from standard oceanographic measurements), the ratio $\hat{a}$ represents a fundamental linkage between scales. It should be noted that combining $\hat{a}$ and $a_*$ yields the entrainment ratio, $E = \frac{w_e}{\Delta u} = \frac{\hat{a}}{a_*}$, often used to characterize turbulent intensity, particularly in early laboratory studies.

## 1.2 Richardson number dependence

Because of difficulties in measuring the gradients in (1) precisely, a practical approach is to consider a bulk Richardson number:

$$Ri_B = g'h(\Delta u)^{-2} \quad (2)$$

where $g' = g\frac{\Delta\rho}{\rho_o}$ is a reduced gravity, representative of a broader portion of the water column. In this case, a higher critical value (often $\boldsymbol{Ri_B}$ on the order of 0.5 - 1) is typically considered (e.g., Fong and Geyer 2001; Pollard et al 1973; Price et al 1986), indicative of the fact that the local $\boldsymbol{Ri_g}$ value is likely to meet the critical condition of 1/4 in isolated regions when the higher bulk threshold is met. Despite the utility of this approach, there is no general agreement on a critical value of $\boldsymbol{Ri_B}$. Turbulence has also long been characterized by the Reynolds number, defined in this context as $\boldsymbol{Re} = h\Delta u/\nu$, which represents the ratio of inertial to viscous forces. Despite the importance of $\boldsymbol{Re}$ in defining the transition from laminar to turbulent flow, it is generally considered of second order importance in predicting important quantities such as the turbulent eddy viscosity, or turbulent velocity scales (expressed here in non-dimensional form as $\hat{a}$ or $\boldsymbol{E}$), once a critical threshold has been surpassed (e.g., Avila et al 2011).

The use of $\boldsymbol{Ri_B}$ as a key diagnostic in the prediction of turbulence remains central to the turbulence closure schemes employed in ocean models (e.g. Large et al, 1994, Umlauf and Burchard 2003; Venayagamorthy et al 2003; Canuto et al 2010), and studies of entrainment also echo the dependence on $\boldsymbol{Ri_B}$, or the related interfacial Froude number, $Fr_o = \Delta u (g'h)^{\frac{1}{2}} = Ri_B^{-\frac{1}{2}}$ (e.g., Wells et al 2010). Frequently, turbulent quantities are also related to parameters such as $Re_T = \frac{ql}{\nu}$, $Fr_T = \frac{q}{Nl}$, and $Re_B = \frac{\varepsilon}{\nu N^2}$ (e.g., Ivey et al 2008; Bouffard and Boegman 2013; Salehipour et al 2016b; Mashayek et al 2017b), which are fundamental ratios based on turbulent length, $l$, and velocity, $q$, scales, or the TKE dissipation rate itself. These parameters typically involve some knowledge of the turbulence field a priori, so their utility in a purely prognostic sense is limited.

Relationships based primarily on $\boldsymbol{Ri_B}$ have also been explored relative to recent DNS studies of stratified shear turbulence (e.g., Shih et al 2000; Smyth et al 2001; Smyth et al 2005; Mashayek and Peltier 2012), which are typically used to simulate relatively low $\boldsymbol{Re}$ flows (i.e. $\boldsymbol{Re} \sim 10^3$-$10^4$). However, the utility of these results, or similar laboratory studies, to higher Reynolds number flows is unclear, and application to larger scales is often performed without the benefit of any existing guidance (e.g. Hetland 2010; Mashayek et al 2017b).

Most measurements of turbulence in ocean and coastal environments (i.e. $\boldsymbol{Re} \sim 10^6$-$10^8$) have been undertaken directly using microstructure techniques (e.g., Lueck et al 2002, Nash et al 2012; Stahr and Sanford 1999; Moum and Osborn 1986; Gargett 1978, Nash et al 2009;

MacDonald et al 2007), or inferred using control volume analyses(e.g. Horner-Devine et al 2013; Kilcher et al 2012; McCabe et al 2008; MacDonald and Geyer 2004; Kay and Jay 2003), or observations of overturn scales (e.g. Orton and Jay 2005; Ferron et al 1998; Dillon 1982), and typically focus on constraining terms in the turbulent kinetic energy (TKE) budget, or estimates of turbulent stress. Ocean measurements typically rely on large ensembles of measurements (MacDonald et al 2013), and cannot provide the detailed mechanistic understanding available from laboratory experiments and DNS modelling. Few attempts have been made to reconcile measurements of turbulence across these extreme ends of the ***Re*** spectrum.

Christodoulo (1986) provides an excellent summary of early efforts to understand and parameterize interfacial mixing as a function of $\boldsymbol{Ri_B}$, including Ellison and Turner (1959), Kato and Phillips (1969), Chu and Vanvari (1976), Pedersen (1980), and others, most of which represent laboratory studies of entrainment processes. More recent laboratory investigations (e.g., Yuan and Horner-Devine 2013; Strang and Fernando 2001) have proven consistent with these earlier efforts. However, it is likely that the data used to form these empirical relationships was influenced by other parameters in addition to $\boldsymbol{Ri_B}$. In particular, data from studies of stratified fjords (Buch 1980; with related data in Buch 1981; Buch 1982) was included in the Christodoulo (1986) assessment, which represent ***Re*** values an order of magnitude higher than the laboratory data.

Following Imberger and Ivey (1991), and MacDonald and Geyer (2004), MacDonald and Chen (2012) proposed a non-dimensional mixing parameter $\xi$, defined as:

$$\xi = \frac{B}{g' \Delta u} \quad (3)$$

Utilizing the flux Richardson number, $Ri_f = \frac{B}{P}$, where $B = -\frac{g}{\rho_o}\overline{w'\rho'}$ represents the buoyancy flux, or conversion of TKE to potential energy through mixing, and $P = -\overline{u'w'}\frac{\partial u}{\partial z}$ is the shear production of TKE (Tennekes and Lumley 1972), this parameter can be rewritten in terms of $\boldsymbol{E}$, or $\hat{a}$, as:

$$\xi = \frac{Ri_f}{Ri_B} a_*^2 E^2 = \frac{Ri_f}{Ri_B} \hat{a}^2 \tag{4}$$

Equation (4) provides a means of directly comparing measurements of $\boldsymbol{E}$ (typically laboratory studies) with measurements of TKE quantities expressed as ξ (typically field measurements), and/or expressing both in terms of the ratio $\hat{a}$. A relationship for $a_*$ based on $\boldsymbol{Ri_B}$(e.g. Christodoulo 1986; Kato and Philips 1969; Pollard, Rhines and Thompson 1973; and Price 1979):

$$a_* = c_1 Ri_B \qquad Ri_B > \sim 10^{-1} \tag{5}$$

$$a_* = c_2 Ri_B^{\frac{1}{2}} \qquad Ri_B < \sim 10^{-1}$$

Independent estimates of both $\boldsymbol{E}$ and ξ are reported for the Fraser River near field plume in MacDonald and Geyer (2004). These two observed values are consistent with the relationships shown in Equations (4) and (5). Additionally, unlike $\hat{a}$ and $\boldsymbol{E}$, $a_*$ is a ratio of two turbulent scales, and does not reflect any bulk flow scales. Thus, we hypothesize that (5) adequately expresses the empirical variability in $a_*$, suggesting that (5) is consistent across large ranges of ***Re***.

$\boldsymbol{Ri_f}$ is often assumed constant at a value of approximately 0.18 to 0.2 (Gregg et al 2018) for stratified shear flows, particularly in the analysis of field observations. Alternatively, DNS evidence suggests that $\boldsymbol{Ri_f}$ varies substantially throughout the evolution and decay of a single

Kelvin Helmholtz billow (Smyth et al 2001; Salehipour and Peltier 2019). The assumption of a constant value of $\boldsymbol{Ri_f}$ for analysing field observations illustrates the inherent issues with extrapolating DNS or laboratory experiments, often focused on an individual overturning event, to the field scale, where water mass modifications are driven by the net impact of many individual events.

Here, we follow Gregg et al (2018) and focus on the integrated effects of many billows resulting in net mixing in the ocean environment. However, a decreasing value of $\boldsymbol{Ri_f}$ under conditions of very low stratification, and thus decreasing $\boldsymbol{Ri_B}$, must be accounted for (e.g., Balmforth et al 1998; Peltier and Caulfield 2003; Venayagamoorthy and Koseff 2016), as stratification is necessary for the conversion of TKE to potential energy. In the analyses that follow, these two observations are represented empirically as:

$$Ri_f = 0.18(1 + 0.01Ri_B^{-2})^{-1} \tag{6}$$

as shown in figure 2. This approximation is restricted to naturally occurring turbulence in stratified shear flows generated through KH instabilities, where the ratio $\frac{L_O}{L_T}$ is of order one. The exact nature of $\boldsymbol{Ri_f}$ variability, particularly at the single overturn scale, remains a subject of open scientific debate (e.g. Lozovatsky and Fernando 2012), and may ultimately depend on the organization of locally critical turbulent patches within the larger flow structure (e.g., Salehipour et al 2018; Smyth et al 2019). However, given the focus of the present analysis on net mixing processes, the parameterization in (6) provides an effective means of addressing the issue of mixing efficiency.

## 1.3 The effect of scale

Unlike $a_*$, the ratio $\hat{a}$ does not appear to be consistent across scales, a characteristic also extended to related variables ξ and $\boldsymbol{E}$. The plot in figure 3 shows turbulence data from a variety of sources, including both laboratory and field data, reduced to $\hat{a}$ and plotted as a function of $\boldsymbol{Ri_B}$. Data represented includes the compiled data utilized by Christodoulo (1986), as well as dashed lines approximating his proposed power law relationships, transformed to $\hat{a}$ using $E = \frac{\hat{a}}{a_*}$, and (5). Additional data has been drawn from field studies referenced in Wells et al (2010) and Cenedese and Adduce (2010), with certain studies (e.g., Girton and Sanford 2003; Peters and Johns 2005; Arneborg et al 2007) removed due to the influence of bottom boundary layers. Likewise, the laboratory data of Cenedese and Adduce (2008) has not been included due to the potential for bottom boundary layer influence. However, recent data from a range of unbounded shear stratified flows, including several recent river plume studies (e.g., MacDonald et al 2007; Kilcher et al 2012), and recent laboratory data from Yuan and Horner-Devine (2013) have been added.

Small scale stratified shear layers are represented in Figure 3 exclusively by laboratory data. DNS studies, which cover a similar parameter space to laboratory studies often focus primarily on the internal dynamics of KH billows or similar instabilities, and rarely report mean, or net, turbulent quantities. DNS results can also be highly sensitive to initial and boundary conditions (Palma 2018), and thus may not always be directly comparable to naturally occurring flows. For example, arbitrary domain lengths for DNS simulations can alter the natural wavelength of KH instabilities and ultimately affect their energetics. Because laboratory experiments result in non-constrained billow evolution, they are used here to represent small scale stratified shear flows. However, carefully initialized and bounded DNS experiments will undoubtedly play an important future role in refining the proposed parameterizations.

Note that the majority of the field data in figure 3 falls one to two orders of magnitude below laboratory data at similar values of $\boldsymbol{Ri_B}$, but that a continuum of $\hat{a}$ values exists spanning the range from approximately $3\mathrm{x}10^{-3}$ to $4\mathrm{x}10^{-1}$. Clearly, the observed variability cannot be attributed solely to $\boldsymbol{Ri_B}$, with $\boldsymbol{Re}$ a logical parameter to explore further, as a representation of scale. In fact, a dimensional analysis for the dependence of unbounded stratified shear turbulence on bulk flow variables and fluid properties (i.e., $h$, $\Delta u$, $g'$, and $\nu$) results in only two independent non-dimensional parameters, $\boldsymbol{Ri_B}$ and $\boldsymbol{Re}$. Although $\boldsymbol{Re}$, which varies for the data shown in figure 3 from $10^2$ to $10^8$, can provide some segregation of the data, no clear relationship is apparent.

The empirical relation proposed by Cenedese and Adduce (2010) suggests a positive correlation between $\boldsymbol{Re}$ and $\boldsymbol{E}$, such that higher $\boldsymbol{Re}$ flows are generally associated with higher entrainment, although this dependence collapses for low values of $\boldsymbol{Ri_B}$. This stands in contrast to the values of $\hat{a}$ (equivalent to $a_* E$) plotted in figure 3. However, the data set explored in Cenedese and Adduce (2010) contained a limited amount of field data at high $\boldsymbol{Re}$, including several experiments which appear to have significant bottom boundary layer influence. Furthermore, the represented field data is biased towards higher values of $\boldsymbol{Ri_B}$, with no observations of ocean scale flows at subcritical $\boldsymbol{Ri_B}$ values. Thus, the decrease in turbulence observed by Cenedese and Adduce (2010) for geophysical scale observations, which they attributed to supercritical $\boldsymbol{Ri_B}$ values (or subcritical Froude numbers) in their parameterization, may, in fact, be attributable to the high $\boldsymbol{Re}$ values associated with these flows.

The distribution of data in figure 3 clearly demonstrates the need for a multi-dimensional parameterization for stratified shear turbulence. Salehipour et al (2016b) describe a multi-dimensional parameterization for the turbulent mixing efficiency in terms of Rig and ReB, similar in some respects to the effort undertaken here, but their parameterization does not address overall scale of the stratified shear layer. Here, the overall layer thickness, $h$, is considered a key parameter in setting the turbulence intensity, as described by $\hat{a}$. The remainder of this manuscript discusses a new approach to parameterizing $\hat{a}$ as a function of both $\boldsymbol{Ri_B}$ and $\boldsymbol{Re}$, using an approach that correlates $\boldsymbol{Re}$ to a ratio of length scales, $\frac{h}{\eta}$. The connection between $\boldsymbol{Re}$ and $\frac{h}{\eta}$ is defined in Section 2 along with an overview of the quasi-empirical approach employed to investigate the proposed relationships. Section 3 proposes specific physical mechanisms linking the length scale ratio to the magnitude of $\hat{a}$, while Section 4 defines the new relationship in terms of a new "Turbulent Geography" that represents the value of $\hat{a}$ in the two-dimensional, $\boldsymbol{Ri_B} - \boldsymbol{Re}$ plane. A summary is provided in Section 5.

## 2. The Case for *Re* Parameterization

As discussed above, the data distribution in figure 3 emphasizes the need for a multi-dimensional parameterization for stratified shear turbulence, and dimensional analysis suggests that $\boldsymbol{Ri_B}$ and $\boldsymbol{Re}$ may be the only relevant bulk scale parameters. Although a multivariate regression could be utilized to predict the value of $\hat{a}$ as a function of $\boldsymbol{Ri_B}$ and $\boldsymbol{Re}$ using the data shown in figure 3, it would lack any valid physical interpretation. Additionally, there are significant gaps of data within the $\boldsymbol{Ri_B} - \boldsymbol{Re}$ parameter space, such that any attempt at a purely statistical regression of the figure 3 data would be poorly constrained. Instead of focusing strictly on the inertial/viscous force comparison inherent in ***Re***, ratios of the shear layer thickness, $h$, to fundamental turbulent length scales are explored.

### 2.1 The $\frac{h}{\eta}$ ratio

In an attempt to compare a turbulent length scale to the layer thickness, $h$, use of the Ozmidov scale as a representative turbulent length scale might appear to be the logical choice. However, utilizing the definition of the Ozmidov scale, $L_O = (\varepsilon N^{-3})^{\frac{1}{2}}$, and Equation (4), the ratio of these two scales can be shown to vary as $\frac{h}{L_o} = Ri_B^{\frac{3}{4}}\left(1 - Ri_f\right)^{-\frac{1}{2}}\hat{a}^{-1}$, which would provide no additional value in the prediction of $\hat{a}$ beyond $\boldsymbol{Ri_B}$ alone. Instead, we focus on the ratio $\frac{h}{\eta}$, which, following a similar derivation, can be related to ***Re*** as:

$$\frac{h}{\eta} = \left(1 - Ri_f\right)^{\frac{1}{4}}\hat{a}^{\frac{1}{2}}Re^{\frac{3}{4}} \qquad (7)$$

The dependence of this ratio on ***Re*** can provide an alternative mechanism for observed variability in $\hat{a}$. Note that in practice, assuming a functionality of $\boldsymbol{Ri_f}$ as described by equation (6), the value of the $\left(1 - Ri_f\right)^{\frac{1}{4}}$ term in equation (7) varies from 0.95 to 1, so that it can effectively be considered negligible.

The Buoyancy Reynolds Number, $Re_b = \frac{\varepsilon}{\nu N^2}$, and a related ratio, $I = \frac{L_O}{\eta} \approx \hat{a}^{\frac{3}{2}}\left(\frac{Re}{Ri_B}\right)^{\frac{3}{4}} = Re_b^{\frac{4}{3}}$, have been used similarly to represent the separation between the smallest and largest turbulent overturns. Bluteau et al (2013) found ***I*** to be moderately effective at predicting mixing efficiencies, and, ultimately turbulent diffusivities, utilizing the models of Shih et al (2005) and

Osborn (1980). This approach, however, lacked skill compared to more direct representations of this scale separation, such as $\boldsymbol{Re_T}$. Here we focus on the ratio $\frac{h}{\eta}$, with its more direct correlation to $\boldsymbol{Re}$, as a means of understanding the separation between turbulent and *environmental* scales. In this context note that (7) can be rewritten as $\frac{h}{\eta} = Re^{\frac{3}{4}}\left(\frac{\varepsilon h}{\Delta u^3}\right)^{\frac{1}{4}}$, where the quantity in parentheses represents the ratio of TKE dissipation to a ratio reminiscent of the inertial scaling of Taylor (e.g. Taylor 1935; Vassilicos 2015). However, in this case, $h$ does not necessarily represent the outer scale of the turbulence, $l$, but the environmental scale of the shear layer.

In figure 4, the data from figure 3 is plotted in $\boldsymbol{Ri_B}$ - $\frac{h}{\eta}$ space. The two panels of figure 5 show more clearly the distribution of the data in the $\boldsymbol{Ri_B}$ - $\frac{h}{\eta}$ plane, and the value of $\hat{a}$ as a function of $\frac{h}{\eta}$. In figure 6, $\hat{a}$ is plotted against $\boldsymbol{Ri_B}$ for both low and high values of $\frac{h}{\eta}$. It should be noted that $\boldsymbol{Re}$ has been approximated for most of the "legacy data" (i.e., Ellison and Turner 1959; Chu and Vanvari 1976; Pedersen 1980; Buch 1980) based on estimates of length and velocity scales that could be inferred from the original manuscripts based on the size of the experimental apparatus or observational context. In these cases, a single representative value has been assigned for each data set. While these estimates are only representative, the likely error in this approach is small compared to the $\boldsymbol{Re}$ parameter space spanning more than five orders of magnitude.

The behaviour of $\hat{a}$ in $\boldsymbol{Ri_B}$ - $\frac{h}{\eta}$ parameter space can be characterized by the following observations gleaned from inspection of figures 3 through 6:

a) $\hat{a}$ decays for $\boldsymbol{Ri_B}$ values below ~ 0.1 (figure 3 and consistent with Christodoulo, 1986).

b) $\hat{a}$ decays for increasing values of $\boldsymbol{Ri_B}$, for turbulence at low values of $\frac{h}{\eta}$, but remains relatively constant with increasing $\boldsymbol{Ri_B}$ for high values of $\frac{h}{\eta}$ (figure 6).

c) $\hat{a}$ is amplified for low values of $\frac{h}{\eta}$ (figure 5).

These observations can be explained by utilizing a "building block" theory, based on a turbulent generation length scale. In the following sections, this theory is explained, proposed mechanisms are highlighted, and a mechanistically driven empirical approach is used to define the behaviour of $\hat{a}$ in $\boldsymbol{Ri_B}$ - $\frac{h}{\eta}$ parameter space.

### 2.2 Turbulent generation length scale theory

A stratified shear flow with a given shear layer thickness, $h$, will become unstable and generate turbulence if the gradient Richardson number, $\boldsymbol{Ri_g}$, becomes subcritical at some point within the shear layer. The length scale across which $\boldsymbol{Ri_g}$ must be subcritical is not defined, but it is clear that it can be less than $h$ (Garg et al 2000), and likely also less than $\boldsymbol{L_o}$, given the effective use of smaller scale velocity perturbations to excite turbulence in DNS simulations (e.g. Smyth et al 2001), and the fact that a classic two-layer flow can spawn overturns significantly larger than the shear layer thickness (e.g., Thorpe 1969). Once initiated, a single turbulent event may grow in scale up to or even exceeding the $\boldsymbol{L_o}$ limit, in the process forcing subcritical $\boldsymbol{Ri_g}$ values in adjacent regions of the shear layer, and thereby perpetuating the growth of the turbulent field. Thus, turbulence in a stratified shear flow can be conceptualized as constructed of turbulent "building blocks" or "cells", with a turbulent generation length scale independent of both $h$ and

$\boldsymbol{L_o}$. Assuming that this "building block" scale is sufficiently small that viscosity, $\nu$, is important, and utilizing $\varepsilon$ as a proxy for available TKE in the system, dimensional analysis can only return the Kolmogorov scale, $\eta$, as an appropriate "building block" scaling. Thus, the ratio $\frac{h}{\eta}$ must be directly proportional to the number of "building blocks" contained within the shear layer. This suggests that the smallest perturbations possible (anything smaller than this scale would be absorbed by internal friction) are responsible for the excitation of turbulence, which grows in size before retreating to a similar scale at the dissipative end of the turbulent cycle.

Consideration of the $\frac{h}{\eta}$ ratio allows for the proposal of mechanisms specific to each of the observations identified above. To accelerate understanding of the overall relationship between $\hat{a}$, $\boldsymbol{Ri_B}$, and $\frac{h}{\eta}$, an empirical function, $\Phi_n$ is defined based on each proposed mechanism, such that $\hat{a}$ can then be predicted as:

$$\hat{a} = \hat{a}_o \Phi_B \Phi_L \Phi_C \tag{8}$$

where $\Phi_B$, $\Phi_L$, and $\Phi_C$ represent functions associated with specific proposed mechanisms which are discussed further in Section 3. Each empirical function is constrained by several coefficients, the values of which are determined by a global least squares fit to the available data. By using a mechanistically driven empirical approach, the functionality of $\hat{a}$ can be explored, while developing a road map for more focused physical analysis of each relationship.

## 3. The Turbulent Generation Mechanisms

### 3.1 The base $\hat{a}$ vs. $\boldsymbol{Ri_B}$ relationship

Figure 6 (a) shows $\hat{a}$ as a function of $\boldsymbol{Ri_B}$ for data with high values of $\frac{h}{\eta}$ only (i.e., $\frac{h}{\eta} >$ 600), representing turbulence that is generally unconstrained by the shear layer boundaries. This plot suggests a relatively constant value of $\hat{a}$ for $\boldsymbol{Ri_B}$ > ~1, and $\hat{a}$ decreasing with decreasing $\boldsymbol{Ri_B}$, for $\boldsymbol{Ri_B}$ < ~1, consistent with observation (a) in Section 2.1. This form is consistent with the hypotheses of Christodoulo (1986), as shown by the dashed line in Figure 3.

A decrease in $\hat{a}$ at low $\boldsymbol{Ri_B}$ is expected due to the decreased importance of stratification in these environments (Forryan et al 2013). Although unstratified, or minimally stratified, fluids are easily mixed, it is this relative ease of mixing that can result in the potentially counterintuitive result of decreased turbulence. Relatively rapid homogenization of the fluid will eliminate the velocity shear necessary to generate turbulence, unless the shear is forced by a boundary layer such as an imposed wind stress, or a no-slip condition along a bottom boundary. Additionally, turbulence in the limit of low stratification may be substantially less energetic because it does not have to overcome the potential energy constraints of the density gradient.

The bold line superimposed on figure 6 (a) is an approximation of the form of the empirical function, $\Phi_B$, designated to represent the observed trends in the base $\hat{a}$ vs. $Ri_B$ relationship:

$$\Phi_{\mathrm{B}} = \left(1 + \frac{1}{m_1 Ri_B^{n_1}}\right)^{-1} \tag{9}$$

Here, $m_1$, which controls the $\boldsymbol{Ri_B}$ value associated with the roll off of $\hat{a}$, and $n_1$, which controls the slope of $\hat{a}$ decay for low $\boldsymbol{Ri_B}$, are coefficients for which best fit values are determined in Section 4.

### 3.2 Decay of $\hat{a}$ For Large $\boldsymbol{Ri_B}$

The second key observation reported in Section 2.1 is the decay of $\hat{a}$ for increasing $\boldsymbol{Ri_B}$ at low values of $\frac{h}{\eta}$, as illustrated by the data plotted in figure 6 (b). As discussed in Section 2.2, we hypothesize that turbulence is initiated across length scales consistent with the building block scale when local values of $\boldsymbol{Ri_g}$ become subcritical. The definition of $\boldsymbol{Ri_B}$ in Equation (2) essentially represents a larger scale perspective of $\boldsymbol{Ri_g}$, or a ratio of the mean gradients, across the entire shear layer thickness, $h$. However, due to natural fluctuations and perturbations related to layering, secondary interfaces, and residual turbulence, the value of $\boldsymbol{Ri_g}$ everywhere is not expected to equal $\boldsymbol{Ri_B}$. Riley and de Bruyn Kops (2003) have discussed the importance of subcritical $\boldsymbol{Ri_g}$ values at some point within the larger structure of a stratified flow in generating turbulence. Thus, the mechanism proposed for this behaviour is statistically based, representing the likelihood that any subset of building blocks within the shear layer meets the critical condition criteria (i.e., a local value of $Ri_g < \frac{1}{4}$). As the thickness of the shear layer increases relative to the building block scale (i.e., larger values of $\frac{h}{\eta}$), the likelihood that a critical condition occurs somewhere in the layer would also increase, as shown in Figure 7(a). Conversely, as the value of $\boldsymbol{Ri_B}$ increases, it becomes less likely that isolated regions of $\boldsymbol{Ri_g}$ will fall below the critical value.

Once a local instability has been triggered within the shear layer, turbulent processes will work towards homogenizing the fluid across a patch with a vertical length scale consistent with $\boldsymbol{L_o}$, resulting in decreased shear and stratification, and generally increasing local values of $\boldsymbol{Ri_g}$ within the patch. However, at the top and bottom edges of this patch, gradients must increase, with a corresponding decrease in local $\boldsymbol{Ri_g}$, in order to match the existing density and velocity profiles above and below the patch (as shown in Figure 7(b)), potentially forcing them into a subcritical condition, and resulting in the spread of turbulence throughout the shear layer. In this manner, turbulence from a single instability may spread, similar to a single spark ultimately leading to a large inferno. However, this spread of turbulence is likely to be damped for larger values of $\boldsymbol{Ri_B}$ if the gradients at the patch edges are not sufficiently increased to reach the critical condition, leading to the observed roll off behaviour.

In order to capture this mechanism empirically, there are two dependencies to consider. First, the value of $\hat{a}$ must roll off for increasing values of $\boldsymbol{Ri_B}$. Second, the value of $\boldsymbol{Ri_B}$ which triggers the roll off must vary with $\frac{h}{\eta}$, such that no roll off occurs at sufficiently high values of $\frac{h}{\eta}$. To accomplish this, two empirical functions are used. $\Phi_L$ describes the "likelihood" mechanism that controls the decay of $\hat{a}$ as a function of $\boldsymbol{Ri_B}$:

$$\Phi_{\mathrm{L}} = \frac{1}{\left(1+m_2\Phi_{\mathrm{LS}}Ri_B^{n_2}\right)} \tag{10}$$

Similar to Equation (9), coefficients $m_2$ and $n_2$ control the rolloff location and slope, respectively. Note that $m_2$ is modified by $\Phi_{LS}$, which defines the scale dependence of the "likelihood" mechanism by adjusting the rolloff location as a function of $\frac{h}{\eta}$:

$$\Phi_{\mathrm{LS}} = \frac{1}{\left(1+m_3\left(\frac{h}{\eta}\right)^{n_3}\right)} \quad (10)$$

An example of $\Phi_{LS}$ is shown in figure 8. This function also exhibits a roll off and is equal to one for values of $\frac{h}{\eta}$ below a certain threshold. This functionality is essential to limit the decay in $\hat{a}$ from occurring for cases where $\boldsymbol{Ri_B}$ is less than the critical value of $\boldsymbol{Ri_g}$. Here, $m_3$ and $n_3$ similarly control rolloff location and slope.

An example of $\Phi_L$ is illustrated by the dashed line in figure 6 (b). This function effectively captures the decay of $\hat{a}$ at large $\boldsymbol{Ri_B}$, but asymptotes to one for low $\boldsymbol{Ri_B}$. Combining $\Phi_L$ with $\Phi_B$ yields the relationship shown by the dash-dot line in figure 6 (b).

### 3.3 Amplification of $\hat{a}$ at small $\frac{h}{\eta}$

The last observation noted in Section 2.1 was the amplification of $\hat{a}$ at low values of $\frac{h}{\eta}$, as seen in figure 5(b). Despite the variability in $\hat{a}$ for values of $\frac{h}{\eta} > 600$, which is also affected by $\boldsymbol{Ri_B}$ variability, we assume that $\hat{a}$ is essentially constant with $\frac{h}{\eta}$ within this portion of parameter space, such that the variability observed is a function of $\boldsymbol{Ri_B}$. As $\frac{h}{\eta}$ decreases, however, a marked increase in $\hat{a}$ is observed. In interpreting figure 5(b), recall that $\boldsymbol{Re}$ has been estimated for several "legacy" studies, and that substantial variability is also described by $\boldsymbol{Ri_B}$.

Here, we invoke a mechanism based on recent efforts to quantify the difference between DNS and geophysical scale turbulence as the result of continuous (in the geophysical case) vs. intermittent (in the DNS case) forcing mechanisms (e.g., Holleman et al 2016; Zhou et al 2017).

Consider growing instabilities in a low $\frac{h}{\eta}$ environment, which are subjected to a temporally varying stress profile as they expand beyond the limits of the stratified shear region, as opposed to instabilities which are wholly embedded in a uniform shear layer, and thus subject to a more continuous forcing profile. This essentially results in an "energy compression" mechanism for low $\frac{h}{\eta}$ regions. In these cases, growth of turbulent billows into the unstratified regions above and below the stratified shear layer is not opposed by a background density gradient, so that most of the energy in the billow collapses back into the shear layer, resulting in an increased energy density within the shear layer. In regions of high $\frac{h}{\eta}$, the growing billows are not influenced by the stratified shear layer boundaries, and the energy is distributed more broadly, as shown in figure 9 (a).

$\Phi_C$ is the empirical function used to capture the variability of this energy compression mechanism:

$$\Phi_C = 1 + \frac{1}{m_4\left(\frac{h}{\eta}\right)^{n_4}} \tag{11}$$

where $m_4$ and $n_4$ similarly describe the upturn location and slope, respectively. An example of $\Phi_C$ is superimposed as the solid line on the data in figure 9(b). Again, the spread of the data is not intended to be wholly described by the solid line representing $\Phi_C$, as much of the variability is the result of the other mechanisms described above, as well as an artifact of the assumption of constant ***Re*** for certain legacy data sets.

## 4. New Turbulent Regime Diagrams

Combining the effects of the base relationship, the likelihood mechanism, and the energy compression mechanism following Eq. (8), the empirical functions presented in Section 3 can be combined to produce a predictive relationship for $\hat{a}$. This expression leaves a total of nine unresolved coefficients ($m_1 - m_4$, $n_1 - n_4$, and $\hat{a}_o$), which are determined using a best fit approach with the existing data set. This was accomplished through an iterative multivariate process with steps of increasing resolution, carried out until the calculated root mean square error asymptotically approached a minimum value. The outcome of this effort yielded the coefficients presented in Table 1, with an $R^2$ value of 0.85. Despite the wide range of coefficient values, the range of the three key empirical functions ($\Phi_B, \Phi_L, \Phi_C$) in Equation (8) indicate comparable impacts on the value of $\hat{a}$ across reasonable representative ranges of $\boldsymbol{Ri_B}$ and $\frac{h}{\eta}$, as shown in Table 2.

A plot of predicted $\hat{a}$ values vs. measured values is shown in figure 10, indicating that almost all predicted data falls within a half order of magnitude of the measured values, which is robust given the accuracy expected of most measurements of turbulence in the ocean environment, as well as the necessity of approximating ***Re*** values for "legacy" data sets. The fact that a strong fit is achieved is not surprising, given the large number of free coefficients in the empirical function analysis. However, the intent of the exercise is not necessarily to provide a function capable of accurate predictions of $\hat{a}$, but rather to explore the shape of the $\hat{a}$ surface in the $\boldsymbol{Ri_B}$ - $\frac{h}{\eta}$, or $\boldsymbol{Ri_B}$ – ***Re***, plane, and its relationship to proposed mechanisms. In this regard, the resulting relationship is sufficient to build intuition about the functionality of $\hat{a}$. However, the consistency of the coefficients, and the shape of the $\Phi_n$ functions, lends further credibility to the analysis.

### 4.1 The $\hat{\boldsymbol{a}}$ surface in the $\boldsymbol{Ri_B}$ - $\boldsymbol{\frac{h}{\eta}}$ plane

Figure 11 shows contours of the $\hat{a}$ surface, using the regression coefficients in Table 1, on the $\boldsymbol{Ri_B} - \frac{h}{\eta}$ plane, with the location of data from figure 3 superimposed. Much like a topographic map, this and subsequent figures can be used to interpret the "geography" of turbulence in this wider parameter space. Several interesting regions are immediately recognized. The peak in $\hat{a}$ near $Ri_B \approx 0.25$ and $\frac{h}{\eta} \approx 300$, labeled as Region I in figure 11, is the focus of most laboratory and DNS experiments. This region represents an optimal balance of stratification and shear, coupled with a sufficiently amplifying value of $\frac{h}{\eta}$, to achieve maximal turbulent energetics.

At higher values of $\frac{h}{\eta}$ (~ $3\text{x}10^3$ to $10^6$) we observe the majority of the field-based data clustered near the top of a steep slope (Region II in figure 11), which falls off to low $\hat{a}$ values for low values of $\boldsymbol{Ri_B}$. Along this slope, we see that the data is distributed with more coastal and estuarine field sites, including the MeRMADE (e.g. MacDonald et al 2007) and RISE (e.g. Kilcher et al 2012) plume studies as well as saline lake underflows (Dallimore et al 2001), lying at the low end of this $\frac{h}{\eta}$ range and larger scale deep ocean overflows, including the Mediterranean (Johnson et al 1994; Barringer and Price 1997) and Faroes (Mauritzen 2005; Fer et al 2010) overflows, occupying the higher end. Note that above a value of $\frac{h}{\eta} \approx 3000$, $\hat{a}$ becomes primarily a function of $\boldsymbol{Ri_B}$, as has been long reflected in turbulence closures (e.g. Burchard and Baumert 1995; Umlauf and Burchard 2005; Canuto et al 2010) for ocean models. This region is reflective of the conditions across most of the unbounded stratified shear flows within the world's oceans, where $\boldsymbol{Ri_B}$ values cluster near ¼ due to inherent feedback mechanisms controlling turbulent evolution, and shear layers are thick enough that turbulent processes are unconstrained by shear layer thickness. The feedback processes driving $\boldsymbol{Ri_B}$ to near a value of ¼ have been recently described in the context of marginal instability (Thorpe and Liu 2009; Smyth and Moum 2013; Howland et al 2018), an equilibrium between forcing mechanisms driving increased velocities (and lower $\boldsymbol{Ri_B}$), and turbulence, which reduces velocity gradients and drives $\boldsymbol{Ri_B}$ values higher.

Above this slope, the analysis suggests a broad plateau (Region III in figure 11), where high $\boldsymbol{Ri_B}$ values dominate across thick shear layers, but turbulence persists due to initiation by localized regions of subcritical $\boldsymbol{Ri_g}$. This region is characterized by a scarcity of data, with the exception of Fjord data (Buch 1980), and the upper limits of the ocean overflow data at the very top of Region II.

At the far left of the turbulent landscape shown in figure 11 (i.e., $\frac{h}{\eta} \leq 10$), a steep increase in $\hat{a}$ is observed for very thin stratified shear layers. Although the contours at this limit should be viewed with extreme caution, due to the lack of data in the region, a dichotomy of flows in this region might be expected. The region with low $\frac{h}{\eta}$ and high $\boldsymbol{Ri_B}$ would be characterized primarily by a small velocity gradient and a small to mid-range layer thickness. In this region, stability, and a lack of turbulence, would be expected. Conversely, the region with low $\frac{h}{\eta}$ and low $\boldsymbol{Ri_B}$ would generally represent conventional two-layer flows, where the boundary between the two water masses is exceedingly narrow, and the influence of the "energy compression" mechanism is maximal. Flows in this actively turbulent region would be necessarily transient, however, with rapid mixing thickening the gradient zone, and forcing the flow to migrate across the turbulent landscape towards equilibrium conditions as suggested by the preponderance of data near Region I and the top of Region II. In this regard, it should be noted that any flow may be migratory, as the effects of mixing modify the environment and thus alter both $\boldsymbol{Ri_B}$ and $\frac{h}{\eta}$. In many cases, the natural environment and forcing mechanisms may result in the flow converging towards one of the equilibrium zones in Regions I, II, or III, and ultimate maintenance of a "marginal instability" environment. In others, initial stratification may be erased by mixing, resulting in a migration of the flow down the Region II slope towards vanishingly small values of $\boldsymbol{Ri_B}$, where the water column becomes homogenized and stratified shear turbulence is not supported.

### 4.2 Other views of the turbulent landscape

Given the ineffectiveness of the $\frac{h}{\eta}$ ratio as a predictive tool, due to its inherent dependence on $\hat{a}$ as well as $\boldsymbol{Re}$, it is useful to recast the empirical equation strictly in terms of $\boldsymbol{Ri_B}$ and $\boldsymbol{Re}$, which can easily be done by resorting to the definition of $\frac{h}{\eta}$ in Equation 7, resulting in the plot of $\hat{a}$ in the $\boldsymbol{Ri_B} - \boldsymbol{Re}$ plane shown in figure 12. As expected, this surface is similar to that shown in figure 11, with the same general regions as described in Section 4.1. Although there is a lack of representative data in this region, it is interesting to note that the valley of low $\hat{a}$ values at high $\boldsymbol{Ri_B}$ values and $\boldsymbol{Re}$ values on the order of $10^4$ is separated from Region III by a steep wall, suggesting a very narrow transition between turbulence suppression and initiation for otherwise "stable" flows at mid-range Reynolds numbers. Of course, without data in this region, this observation is purely speculative, but suggests an interesting region for further study.

The surface in figure 12 is also superimposed with contours of the Buoyancy Reynolds Number, $Re_b = \frac{\varepsilon}{\nu N^2}$, which is frequently invoked as an indicator of fully three-dimensional turbulence, and an important parameter for scaling stratified shear turbulence (e.g. Maffiolli and Davidson 2016; Bartello and Tobias 2013; Smyth and Moum 2000). An inspection of these contours shows some interesting alignment with the $\hat{a}$ contours, particularly near the steep wall at the low $\boldsymbol{Re}$ boundary of Region III, but in general suggest little predictive capacity with regards to $\hat{a}$. This is likely a reflection of the fact that the values of $\boldsymbol{Re_b}$ calculated here are based on bulk values of dissipation and buoyancy frequency across the entire stratified shear layer, rather than localized across turbulent events, which is the mode commonly employed for interpretation of $\boldsymbol{Re_b}$. In the bulk sense, the value of $\boldsymbol{Re_b}$ may lose meaning given the relationship of the overall layer to the turbulent generation length scale as characterized by the "likelihood mechanism" of figure 7.

Figure 13 shows the surface of ξ, derived from $\hat{a}$ using Equations (4) and (6) in the $\boldsymbol{Ri_B}$ – $\boldsymbol{Re}$ plane. While many regions remain similar to $\hat{a}$, the most notable exception is the decay of ξ with increasing $\boldsymbol{Ri_B}$ across Region III. This occurs because of the influence of $\boldsymbol{Ri_B}$, representing the strength of the density gradient, in Equation (4). In essence, flow environments which populate Region III are effective at producing TKE (and thus high values of $\hat{a}$), but the scale of the turbulence is inefficient to accomplish significant mixing due to the relative thickness of the layer and the resulting density gradient resulting low values of B, and ξ. Hence, the turbulent energy is dissipated without substantially altering the overall structure of the flow.

## 5. Summary

The effort presented here provides a new proposed regime diagram for turbulence in the $\boldsymbol{Ri_B} - \boldsymbol{Re}$ plane and presents a mechanistic explanation for the observed phenomena. Much like 16$^{th}$ century maps of the New World, this new geography is likely a crude representation of the actual landscape, however it provides the basis for further exploration. Furthermore, rather than focusing on a bottom up approach to understanding turbulence by exploring phenomena at the smallest scales, it emphasizes the value of a top down approach based on bulk variables to provide effective parameterization of turbulence in unbounded stratified shear environments. Ultimately, this is in alignment with turbulence closure techniques which, by definition, must predict turbulent parameters at small scales from larger scale flow variables. It should also be noted that the analysis discussed here is focused primarily on oceanic turbulence, although the basic principles should also apply to atmospheric turbulence (e.g. Lozovatsky and Fernando).

An understanding of the new regimes presented here may lead to improved parameterizations and closures at smaller scales, particularly the laboratory and transitional scales below $\boldsymbol{Re} \sim 10^5$ - $10^6$. As computational power increases, allowing models of increasing resolution to simulate flows in complicated coastal bathymetries, such closures may be essential to provide accurate simulations. Furthermore, an understanding of the new regimes will help to bridge the gap between DNS models, which are rarely run at $\boldsymbol{Re}$ values higher than $\sim 10^4$, and real ocean flows.

The new regimes presented here, and the proposed mechanisms upon which they are based, may ultimately help to provide new answers to old turbulence questions.

- How is turbulence generated and maintained at high values of $\boldsymbol{Ri_B}$? The "likelihood mechanism" of figure 7, built on the idea of a fundamental length scale responsible for the generation of turbulence, provides a starting point.
- What is the most meaningful scale to calculate $\boldsymbol{Ri_g}$? When this scale is consistent with the overall layer thickness, the likelihood of generating turbulence within the layer at values of $\boldsymbol{Ri_B}$ above ¼ should fall off dramatically. Based on figure 11, a value on the order of $\frac{h}{\eta} \sim 10^2$ might best represent this range, suggesting that the appropriate $\boldsymbol{Ri_g}$ length scale might be on the order of $100\eta$. Presumably this scale is also representative of the turbulent generation length scale. Assuming representative TKE dissipation rates on the order of $10^{-4}$ W/Kg at the laboratory scale (e.g. Yuan and Horner-Devine 2013), $10^{-3}$ W/Kg in a near field river plume (e.g., MacDonald et al 2007), and $10^{-6}$ W/Kg in a large scale ocean overflow (e.g., Mauritzen et al 2005), the appropriate length scales for calculating $\boldsymbol{Ri_g}$ would then be on the order of 3 cm, 2 cm, and 10 cm, respectively. Although these values appear reasonable, this issue would clearly benefit from further study.
- What is a critical value for $\boldsymbol{Ri_B}$? Clearly, this depends on scale. A reasonable starting point may be the line following the top of the steep wall that bounds Region III, as illustrated by the bold dashed line in figure 12. This line suggests a critical value of $\boldsymbol{Ri_B}$ on the order of 1 to 10 for laboratory scales and approaching 100 or higher at geophysical scales. Note that this line does not extend beyond the point where the layer thickness, $\boldsymbol{h}$, is on the order of the turbulent generation length scale (i.e., $\frac{h}{\eta} \sim 10^2$), as discussed above.

In summary, the mechanistically based empirical analysis described here has provided insight into the continuum of stratified shear turbulence from laboratory to geophysical scales. Further efforts to refine these relationships may prove worthwhile.

## Acknowledgements:

The author wishes to thank Mathew Wells, Lou Goodman, and Mehdi Raessi for invaluable discussions and feedback on initial drafts of this manuscript, and Anneliese Schmidt for assistance in compiling literature data. This work was funded by Office of Naval Research grants N00014-15-1-2456 and N00014-16-1-2441. There are no new data presented in the mansuscript.

## References:


Arneborg, L., V. Fiekas, L. Umlauf, and H. Burchard, 2007: Gravity current dynamics and entrainment—–A process study based on observations in the Arkona Basin. J. Phys. Oceanogr., 37, 2094–2113.

Avila, K., D. Moxey, A. de Lozar, M. Avila, D. Barkley, B. Hof, 2011. The Onset of Turbulence in Pipe Flow, Science, Vol. 333 (6039), pp 192-196 [doi: 10.1126/science.1203223]

Balmforth, N.J., S.G. Llewellyn Smith, and W.R. Young 1998. Dynamics of interfaces and layers in a stratified turbulent fluid. J. Fluid Mech. 355:329–58

Baringer, M. O., and J. F. Price, 1997: Mixing and spreading of the Mediterranean outflow. J. Phys. Oceanogr., 27, 1654–1677.

Bartello, P. and S.M. Tobias, 2013: Sensitivity of stratified turbulence to the buoyancy Reynolds number. Journal of Fluid Mech. Vol. 725, pp. 1-22.

Bluteau, C. E., N. L. Jones, and G. N. Ivey (2013), Turbulent mixing efficiency at an energetic ocean site, J. Geophys. Res.Oceans, 118, 4662–4672, doi:10.1002/jgrc.20292.

Bouffard, D. and L. Boegman, 2013: A diapycnal diffusivity model for stratified environmental flows. Dyn. Atmos. Ocean, 61–62, pp. 14-34. https://doi.org/10.1016/j.dynatmoce.2013.02.002

Buch, E., 1980: On entrainment and vertical mixing in stably stratified fjords, Proceedings, 2nd International Symposium on Stratified Flows, Trondheim.

Buch, E., 1981: On entrainment observed in laboratory and field experiments, Tellus, vol. 34, pp. 307-311.

Buch, E., 1982: On entrainment and vertical mixing in stably stratified fjords, Estuarine, Coastal and Shelf Science, vol. 12, pp. 461-469.

Burchard, H., Baumert, H., 1995. On the performance of a mixed-layer model based on the k2e turbulence closure. Journal of Geophysical Research 100, 8523–8540.

Carr, J., G. Mariotti, S. Fahgerazzi, K. McGlathery, P. Wiberg, 2018. Exploring the Impacts of Seagrass on Coupled Marsh-Tidal Flat Morphodynamics. Frontiers in Environmental Science 6, 92. DOI 10.3389/fenvs.2018.00092.

Cenedese C. and Adduce C., 2008. Mixing in a density-driven current flowing down a slope in a rotating fluid. J. Fluid Mech., 604, 369-388.

Cenedese C. and Adduce C., 2010. A new parameterization for entrainment in overflows. J. Phys. Oceanogr., 40, 1835-1850.

Christodoulou, G.C., (1986): Interfacial mixing in stratified flows. Journal of Hydraulic Research, vol. 24(2), 77-92.

Chu, V.H., and M.R. Vanvari, 1976: Experimental study of turbulent stratified shearing flow. J. Hydraulics Div., ASCE, Vol. 102, No. HY6.

Dallimore, C. J., J. Imberger, and T. Ishikawa, 2001: Entrainment and turbulence in saline underflow in Lake Ogawara. J. Hydraul. Eng., 127, 937–948.

Dillon, T.M. (1982), Vertical overturns: A comparison of Thorpe and Ozmidov length scales. J. Geophys. Res., 87: 9601-9613.

Ellison, T.H. and J.S. Turner, 1959: Turbulent entrainment in stratified flows. J. Fluid Mechanics, vol. 6, 423-448.

Fer, I., G. Voet, K. S. Seim, B. Rudels, and K. Latarius, 2010: Intense mixing of the Faroe Bank Channel overflow. Geophys. Res. Lett., 37, L02604, doi:10.1029/2009GL041924.

Ferron, B., H. Mercier, K. Speer, A. Gargett, and K. Polzin (1998), Mixing in the Romanche Fracture Zone, J. Phys. Oceanogr., 28, 1929– 1945.

Forryan, A., A. P. Martin, M. A. Srokosz, E. E. Popova, S. C. Painter, and A. H. H. Renner (2013), A new observationally motivated Richardson number based mixing parametrization for oceanic mesoscale flow, J. Geophys. Res. Oceans, 118, 1405–1419, doi:10.1002/jgrc.20108.

Garg, R.P., J. H. Ferziger, S. G. Monismith, and J. R. Koseff, "Stably stratified turbulent channel flows. I. Stratification regimes and turbulence suppression mechanism," Phys. Fluids 12, 2569–2594 (2000).

Gargett, A.E. 1978: Microstructure and finestructure in an upper ocean frontal regime. J. Geophys. Res., 83(C10), pp. 5123-5133.

Geyer, W.R., A.C. Lavery, M.E. Scully, and J.H. Trowbridge, 2010: Mixing by shear instability at high Reynolds number. Geophys. Res. Letters, Vol. 37, L22607, doi:10.1029/2010GL045272.

Girton, J. B., and T. B. Sanford, 2003: Descent and modification of the overflow plume in Denmark Strait. J. Phys. Oceanogr., 33, 1351–1364.

Gregg, M. C. (1987), Diapycnal mixing in the thermocline: A review, J. Geophys. Res., 92(C5), 5249–5286, doi:10.1029/JC092iC05p05249.

Gregg, M., E. D'Asaro, J. Riley, and E. Kunze, 2018: Mixing efficiency in the ocean. Annu. Rev. Mar. Sci., 10, 443–473, https://doi.org/10.1146/annurev-marine-121916-063643.

Hetland, R. D. (2010), The effects of mixing and spreading on density in near-field river plumes, Dyn. Atmos. Oceans, 49, 37–53, doi:10.1016/j.dynatmoce.2008.11.003.

Holleman R, Geyer W, Ralston D. 2016. Stratified turbulence and mixing efficiency in a salt wedge estuary. J. Phys. Oceanogr. 46:1769–83

Horner-Devine, A.R., C.C. Chickadel, and D.G. MacDonald, 2013. Coherent structures and mixing at a river plume front. Chapter in Coherent Flow Structures at the Earth's Surface, J.G. Venditti, J. Best, M. Church and R.J. Hardy, eds. Wiley-Blackwell. ISBN: 978-1-119-96277-9.

Howard, L.N. (1961), Note on a paper by John Miles. J. Fluid Mech. 10, 509–512.

Howland, C.J., J.R. Taylor and C.P. Caulfield, 2018. Testing linear marginal stability in stratified shear layers. J. Fluid Mech., 839, R4, doi:10.1017/jfm.2018.79.

Imberger, J. and G.N. Ivey, (1991): On the nature of turbulence in a stratified fluid. Part II: application to lakes. J. Physical Oceanography, vol. 21, 659-680.

Ivey, G. N., and J. Imberger (1991), On the nature of turbulence in a stratified fluid: I. The energetics of mixing, J. Phys. Oceanogr., 21, 650– 658.

Ivey, G.N., K.B. Winters, and J.R. Koseff, 2008. Density stratification, turbulence, but how much mixing? Annu. Rev. Fluid Mech.40:169–84

Johnson, G. C., R. G. Lueck, and T. B. Sanford, 1994: Stress on the Mediterranean outflow plume. Part II: Turbulent dissipation and shear measurements. J. Phys. Oceanogr., 24, 2084–2092.

Kato, H. and O.M. Phillips, 1969: On the penetration of a turbulent layer into a stratified fluid. J. Fluid Mechanics, Vol. 37, (4).

Kay, D. J., and D. A. Jay (2003), Interfacial mixing in a highly stratified estuary: 2. A ‘‘method of constrained differences’’ approach for the determination of the momentum and mass balances and the energy of mixing, J. Geophys. Res., 108(C3), 3073, doi:10.1029/2000JC000253.

Kilcher, L. F., J. D. Nash, and J. N. Moum (2012), The role of turbulence stress divergence in decelerating a river plume, J. Geophys. Res., 117, C05032, doi:10.1029/2011JC007398.

Lawrence, G. A., Tedford, E. W. and Carpenter, J. R. (2013). Instabilities in Stratified Shear Flow. In Coherent Flow Structures at Earth's Surface (eds J. G. Venditti, J. L. Best, M. Church and R. J. Hardy). doi:10.1002/9781118527221.ch5

Lozovatsky ID, Fernando HJS. 2013 Mixing efficiency in natural flows. Phil Trans R Soc A 371: 20120213. http://dx.doi.org/10.1098/rsta.2012.0213

Lueck R.G., F. Wolk, and H. Yamazaki (2002), Oceanic velocity microstructure measurements in the 20th century, J. of Oceanography, 58, 153-174.

MacDonald, D. G., and F. Chen (2012), Enhancement of turbulence through lateral spreading in a stratified-shear flow: Development and assessment of a conceptual model, J. Geophys. Res., 117, C05025, doi:10.1029/2011JC007484.

MacDonald, D. G., and W. R. Geyer (2004), Turbulent energy production and entrainment at a highly stratified estuarine front, J. Geophys. Res., 109(C5), C05004, doi:10.1029/2003JC002094.

MacDonald, D. G., L. Goodman, and R. D. Hetland (2007), Turbulent dissipation in a near-field river plume: A comparison of control volume and microstructure observations with a numerical model, J. Geophys. Res., 112, C07026, doi:10.1029/2006JC004075.

MacDonald, D.G., J.O. Carlson, and L. Goodman, 2013. On the heterogeneity of shear-stratified turbulence: Observations from a near-field river plume. J. Geophys. Res. Oceans, 118, 6223-6237. DOI: 10.1002/2013JC008891.

Maffioli, A. & P.A. Davidson, 2015. Dynamics of stratified turbulence decaying from a high buoyancy Reynolds number. J. Fluid Mech.786, 210–233.

Mashayek, A., and W. R. Peltier (2011), Turbulence transition in stratified atmospheric and oceanic shear flows: Reynolds and Prandtl number controls upon the mechanism, Geophys. Res. Lett., 38, L16612, doi: 10.1029/2011GL048542.

Mashayek, A. and W. Peltier (2012). The zoo of secondary instabilities precursory to stratified shear flow transition. Part 1 shear aligned convection, pairing, and braid instabilities. Journal of Fluid Mechanics, 708:5–44.

Mashayek, A., C.P. Caulfield, and W. Peltier (2017a). Role of overturns in optimal mixing in stratified mixing layers. Journal of Fluid Mechanics, 826:522–552.

Mashayek, A., Salehipour, H., Bouffard, D., Caulfield, C.P., Ferrari, R., Nikurashin, M., Peltier, W. R. & Smyth, W. D. (2017b) Efficiency of turbulent mixing in the abyssal ocean circulation. Geophys. Res. Lett. 44 (12), 6296–6306.

Mauritzen, C., J. F. Price, T. B. Sanford, and D. Torres, 2005: Circulation and mixing in the Faroese Channels. Deep-Sea Res. I, 52, 883–913.

McCabe, R., B. M. Hickey, and P. MacCready (2008), Observational estimates of entrainment and vertical salt flux in the interior of a spreading river plume, J. Geophys. Res., 113, C08027, doi:10.1029/2007JC004361.

Miles, J.W. (1961). On the stability of heterogeneous shear flows. J. Fluid Mech., 10, 496–508.

Moum, J. N. and T. R. Osborn (1986): Mixing in the main thermocline. J. Phys. Oceanogr., 16, 1250–1259.

Nash, J.D., H. Peters, S.M. Kelly, J.L. Pelegri, M. Emelianov, and M. Gasser, 2012: Turbulence and high-frequency variability in a deep gravity current outflow, Geophys. Res. Lett., 39, doi:10.1029/2012GL052899.

Nash, J.D., L. Kilcher, and J.N. Moum (2009): The structure and composition of a highly-stratified, tidally-pulsed river plume. J. Geophys. Res., 114, C00B12, doi:10.1029/2008JC005036, 2009

Odier, P., J. Chen, M.K. Rivera, and R.E. Ecke, 2009: Fluid mixing in stratified gravity currents: the Prandtl mixing length, Phys. Rev. Letters, 102, 134504, doi: 10.1103/PhysRevLett.102.134504

Orton, P. M., and D. A. Jay (2005), Observations at the tidal plume front of a high-volume river outflow, Geophys. Res. Lett., 32, L11605, doi:10.1029/2005GL022372.

Osborn, T. R. (1980), Estimates of the local rate of vertical diffusion from dissipation measurements, J. Phys. Oceanogr., 10 (1), 83–89.

Palma, V.B., 2018. The effect of domain length and initialization noise on DNS simulations of shear stratified turbulence. MS Thesis. University of Massachusetts Dartmouth.

Pedersen, F.B., 1980: A monograph on turbulent entrainment and friction in a two-layer stratified flow, Inst. Of Hydrodynamics and Hydraulic Eng. Techn. U. Denmark, Series Paper No. 25.

Peltier, W.R. and C.P. Caulfield, 2003: Mixing Efficiency in Stratified Flows. Annu. Rev. Fluid Mech. 2003. 35:135–67 doi: 10.1146/annurev.fluid.35.101101.161144

Peters, H., and W. E. Johns, 2005: Mixing and entrainment in the Red Sea outflow plume. Part II: Turbulence characteristics. J. Phys. Oceanogr., 35, 584–600.

Pollard, R.T., P.B. Rhines, and R.O.R.Y. Thompson, 1973: The deepening of the wind-mixed layer. Geophysical Fluid Dynamics, Vol. 3.

Price, J.F., 1979: On the scaling of stress-driven entrainment experiments, J. Fluid Mech., Vol. 90 (3).

Price, J. F., R. A. Weller, and R. Pinkel, 1986: Diurnal cycling: Observations and models of the upper ocean response to diurnal heating, cooling, and wind mixing, J. Geophys. Res., 91, 8411-8427.

Riley, J. J. and de Bruyn Kops, S. M. (2003). Dynamics of turbulence strongly influenced by buoyancy. Phys. Fluids, 15:2047.

Salehipour, H., Caulfield, C., & Peltier, W. (2016a). Turbulent mixing due to the Holmboe wave instability at high Reynolds number. *Journal of Fluid Mechanics*, 803, 591-621. doi:10.1017/jfm.2016.488

Salehipour, H., W. R. Peltier, C. B. Whalen, and J. A. MacKinnon (2016b), A new characterization of the turbulent diapycnal diffusivities of mass and momentum in the ocean, *Geophys. Res. Lett*., 43, 3370–3379, doi:10.1002/2016GL068184.

Salehipour, H., Peltier, W., & Caulfield, C. (2018). Self-organized criticality of turbulence in strongly stratified mixing layers. Journal of Fluid Mechanics, 856, 228-256. doi:10.1017/jfm.2018.695

Salehipour, H. and W. Peltier (2019). Deep learning of mixing by two ‘atoms’ of stratified turbulence. Journal of Fluid Mechanics, 861, R4, doi:10.1017/jfm.2018.980

Shih, L. H., J. R. Koseff, G. N. Ivey, and J. H. Ferziger (2005), Parameterization of turbulent fluxes and scales using homogeneous sheared stably stratified turbulence simulations, J. Fluid Mech., 525, 193–214, doi:10.1017/S0022112004002587.

Smyth, W.D., and W. R. Peltier (1990) Three-dimensional primary instabilities of a stratified, dissipative, parallel flow, Geophysical & Astrophysical Fluid Dynamics, 52:4, 249-261, DOI: 10.1080/03091929008219506

Smyth, W. D., J. N. Moum, and D. R. Caldwell (2001), The efficiency of mixing in turbulent patches: Inferences from direct simulations and microstructure observations, J. Phys. Oceanogr., 31(8), 1969–1992, doi:10.1175/1520-0485(2001)031.

Smyth, W.D. and J.N. Moum, 2000. Length scales of turbulence in stably stratified mixing layers. Phys. Fluids 12 (6), 1327–1342.

Smyth, W.D., J.D Nash and J.N. Moum, 2005: Differential diffusion in breaking Kelvin-Helmholtz billows, J. Phys. Oceanogr. 35 (6), 1004-1022.

Smyth. W.D. and J.N. Moum, 2013. Marginal instability and deep cycle mixing in the eastern equatorial Pacific Ocean. Geophys. Res. Lett., 40, 1-5, doi:10.1002/2013GL058403.

Smyth, W. D. and Nash, J. D. and Moum, J. N., 2019. Self-organized criticality in geophysical turbulence. Scientific Reports, 9(1), 3747.

Stahr, F. R. and T.B. Sanford, 1999: Transport and bottom boundary layer observations of the North Atlantic Deep Western Boundary Current at the Blake Outer Ridge, Deep-Sea Res. Pt. II, 46, 205– 243, 1999.

Strang, E.J. and H.J.S. Fernando, 2001: Entrainment and mixing in stratified shear flows. J. Fluid Mech., Vol. 428, pp. 349-386.

Taylor GI. 1935. Statistical theory of turbulence. *Proc. R. Soc. Lond. A* 151:421–44

Tennekes, H. and Lumley, J. L. (1972). A first course in turbulence. MIT press.

Thorpe, S. A. (1969), Experiments on the Stability of Stratified Shear Flows, Radio Sci., 4(12), 1327–1331, doi:10.1029/RS004i012p01327.

Thorpe, S., and Z. Liu, 2009: Marginal instability? J. Phys. Oceanogr., 39, 2373–2381, doi:10.1175/2009JPO4153.1.

Umlauf, L., and H. Burchard, 2003: A generic length-scale equation for geophysical turbulence models, J. Mar Res., 61, pp. 235-265.

Vassilicos, J. C. 2015 Dissipation in turbulent flows. *Annu. Rev. Fluid Mech.* **47**, 95–114.

Venayagamoorthy, S. K., Koseff, J. R., Ferziger, J. H., and Shih, L. H., 2003. Testing of RANS turbulence models for stratified flows based on DNS data, Annual Research Briefs, Center for Turbulence Research, NASA-AMES, pp 127-138.

Venayagamoorthy, S.K. and J.R. Koseff, 2016: On the flux Richardson number in stably stratified turbulence. J. Fluid Mech., vol. 798, R1, doi:10.1017/jfm.2016.340

Wells, M., C. Cenedese, and C.P. Caulfield, 2010: The relationship between Flux Coefficient and Entrainment Ratio in Density Currents, J. Phys. Oceanogr., 40, 2713–2727. doi: DOI: 10.1175/2010JPO4225.1

Yuan, Yeping, Alexander R. Horner-Devine, 2013: Laboratory Investigation of the Impact of Lateral Spreading on Buoyancy Flux in a River Plume. J. Phys. Oceanogr., 43, 2588–2610. doi: http://dx.doi.org/10.1175/JPO-D-12-0117.1

Zhou, Z., X. Yu, T.-J. Hsu, F. Shi,W. R. Geyer, and J. T. Kirby (2017), On hydrostatic coastal model simulations of shear instabilities in a stratified shear flow at high Reynolds number, J. Geophys. Res. Oceans, 122,3081–3105, doi:10.1002/2016JC012334.

| Coefficient | Value | Description |
|---|---|---|
| $\hat{a}_o$ | 1.40 x $10^{-2}$ | Base $\hat{a}$ value |
| $m_1$ | 4.83 x $10^{0}$ | Rolloff control for $\Phi_B$ |
| $m_2$ | 1.95 x $10^{4}$ | Rolloff control for $\Phi_L$ |
| $m_3$ | 1.92 x $10^{-8}$ | Rolloff control for $\Phi_{LS}$ |
| $m_4$ | 2.95 x $10^{-10}$ | Rolloff control for $\Phi_C$ |
| $n_1$ | 9.67 x $10^{-1}$ | Slope control for $\Phi_B$ |
| $n_2$ | 5.59 x $10^{-1}$ | Slope control for $\Phi_L$ |
| $n_3$ | 4.50 x $10^{0}$ | Slope control for $\Phi_{LS}$ |
| $n_4$ | 3.06 x $10^{0}$ | Slope control for $\Phi_C$ |

**Table 1:** Coefficients for empirical functions derived from iterative least squares analysis.

| Function | Range |
|---|---|
| $\Phi_B$ | **5 x $10^{-2}$ – 1 x $10^{0}$** |
| $\Phi_L$ | **1 x $10^{-3}$ – 1 x $10^{0}$** |
| $\Phi_C$ | **1 x $10^{0}$ – 3 x $10^{3}$** |

**Table 2:** Range of empirical functions utilizing coefficients shown in Table 1 with representative ranges of $\boldsymbol{Ri_B}$ = [$10^{-2}$ $10^{2}$] and $\frac{h}{\eta}$ = [$10^{2}$ $10^{5}$].

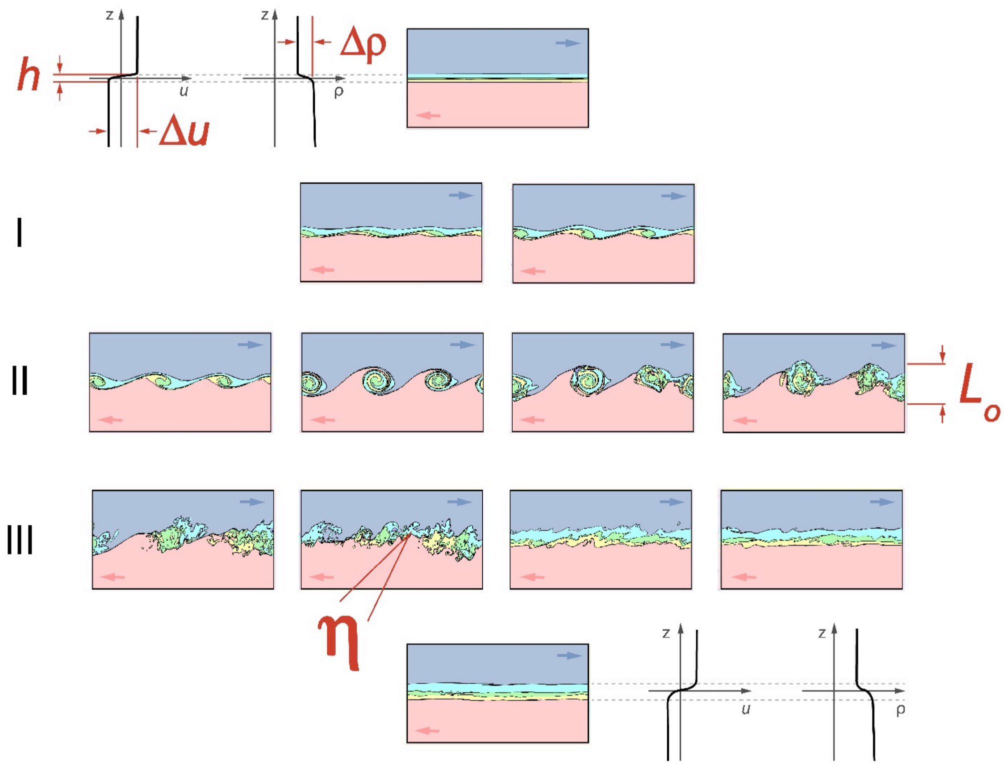


**Figure 1:** Progression of Kelvin-Helmholz billow evolution, from sheared flow (top) through (I) initial perturbation (II) generation of unstable billows and (III) the collapse to homogeneous turbulence, ultimately resulting in a broadening of the mixed layer (bottom) as the turbulence subsides. Relevant length, density, and velocity scales, as described in the text, are illustrated on the figure.

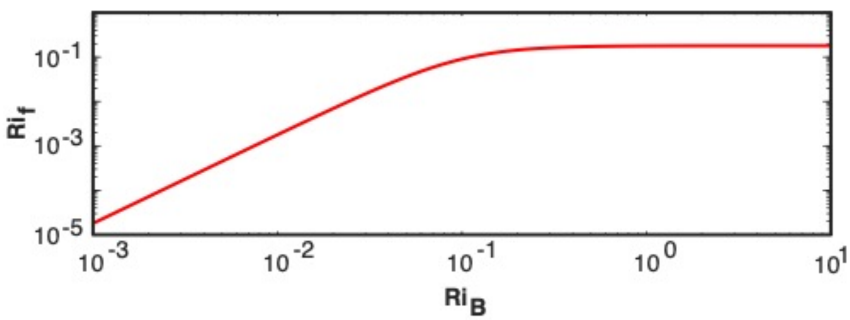


**Figure 2:** Simplified empirical relationships for $\boldsymbol{Ri_f}$ as a function of $\boldsymbol{Ri_B}$, based on Equation (5).

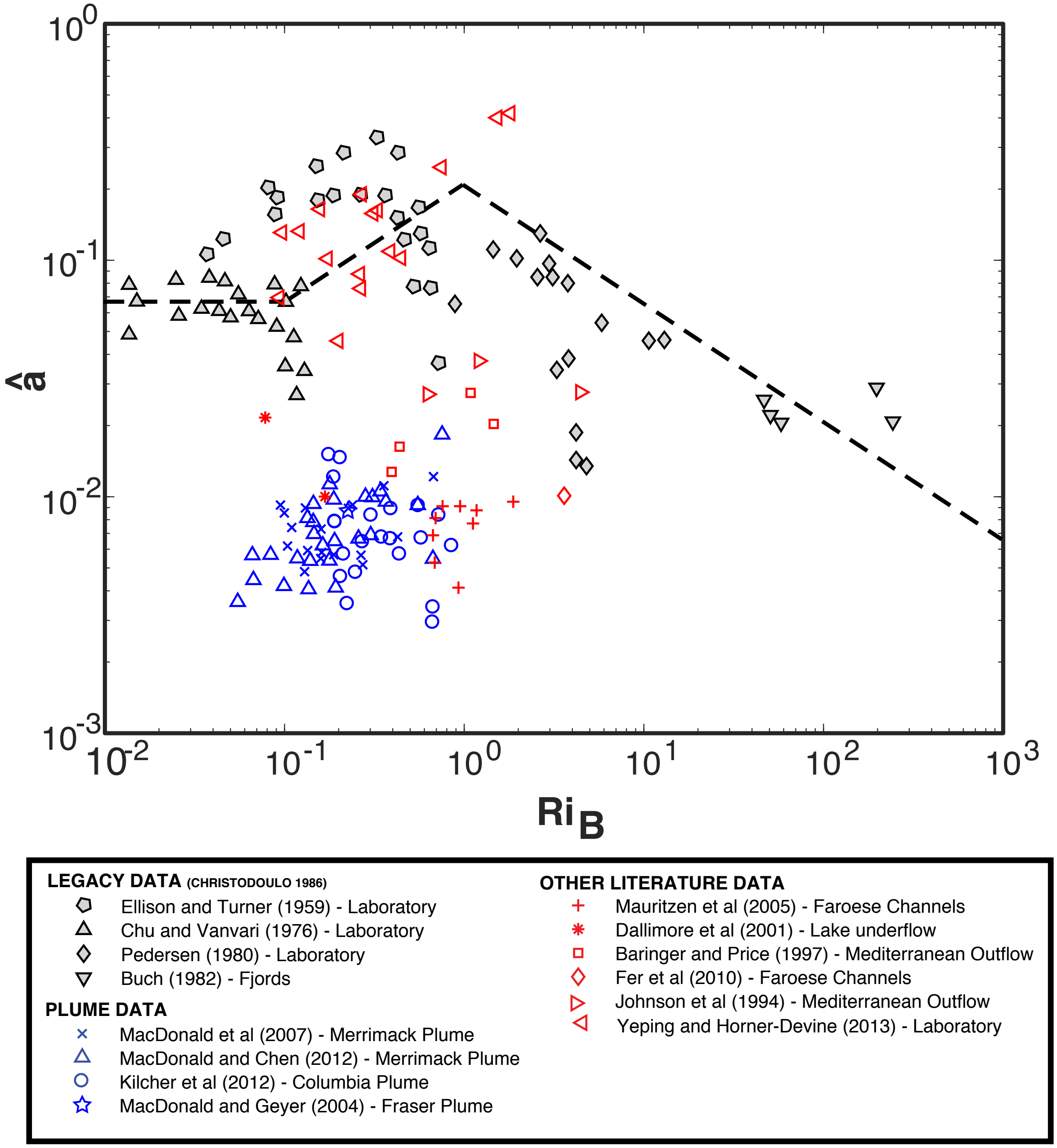


**Figure 3:** Plot of $\hat{a}$ vs. $\boldsymbol{Ri_B}$ for data from identified sources, representing laboratory, river plume, and ocean overflow environments. Dashed lines are consistent with the slope of the proposed power law relationships of Christodoulo (1986), as modified by Equation (4).

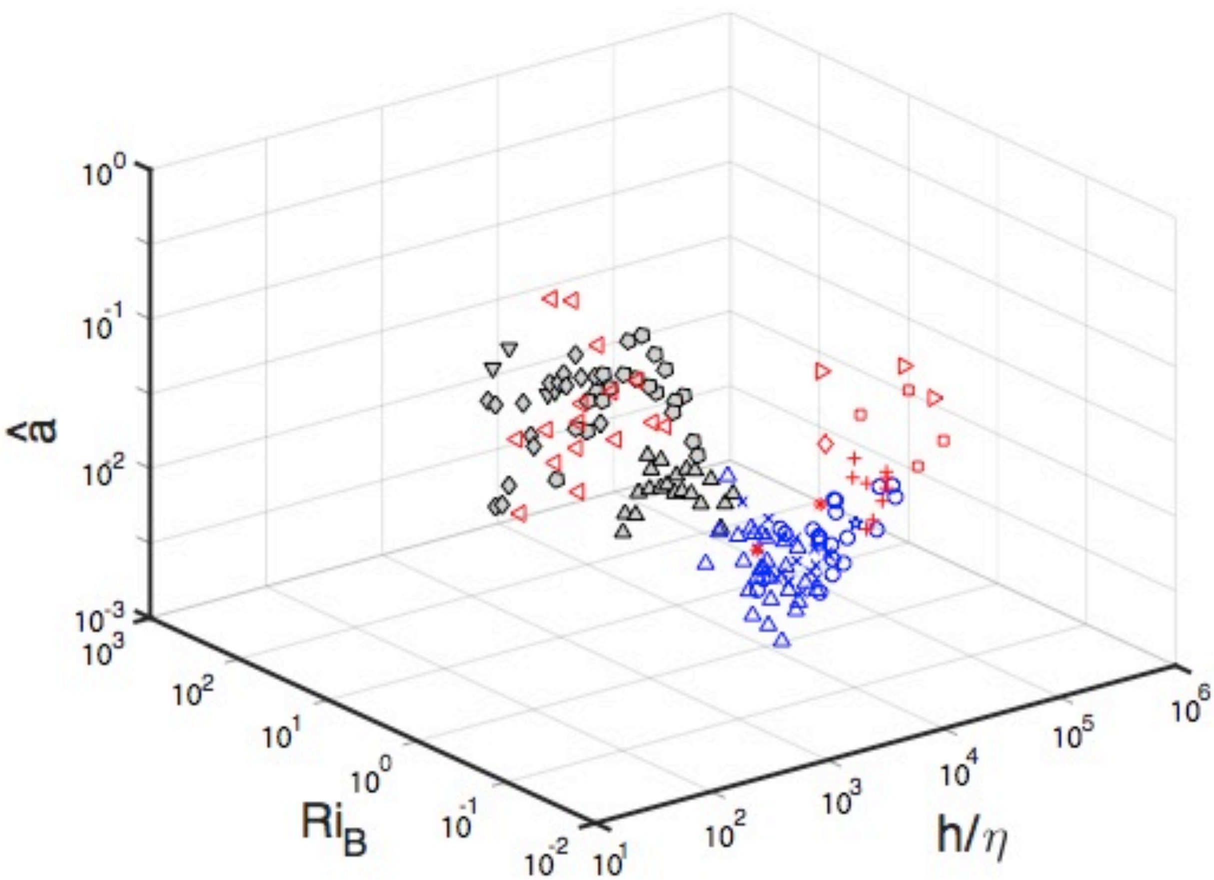


**Figure 4:** Three dimensional plot of $\hat{a}$ in $\boldsymbol{Ri_B}$ - $\frac{h}{\eta}$ parameter space. Legend as shown in Figure 3.

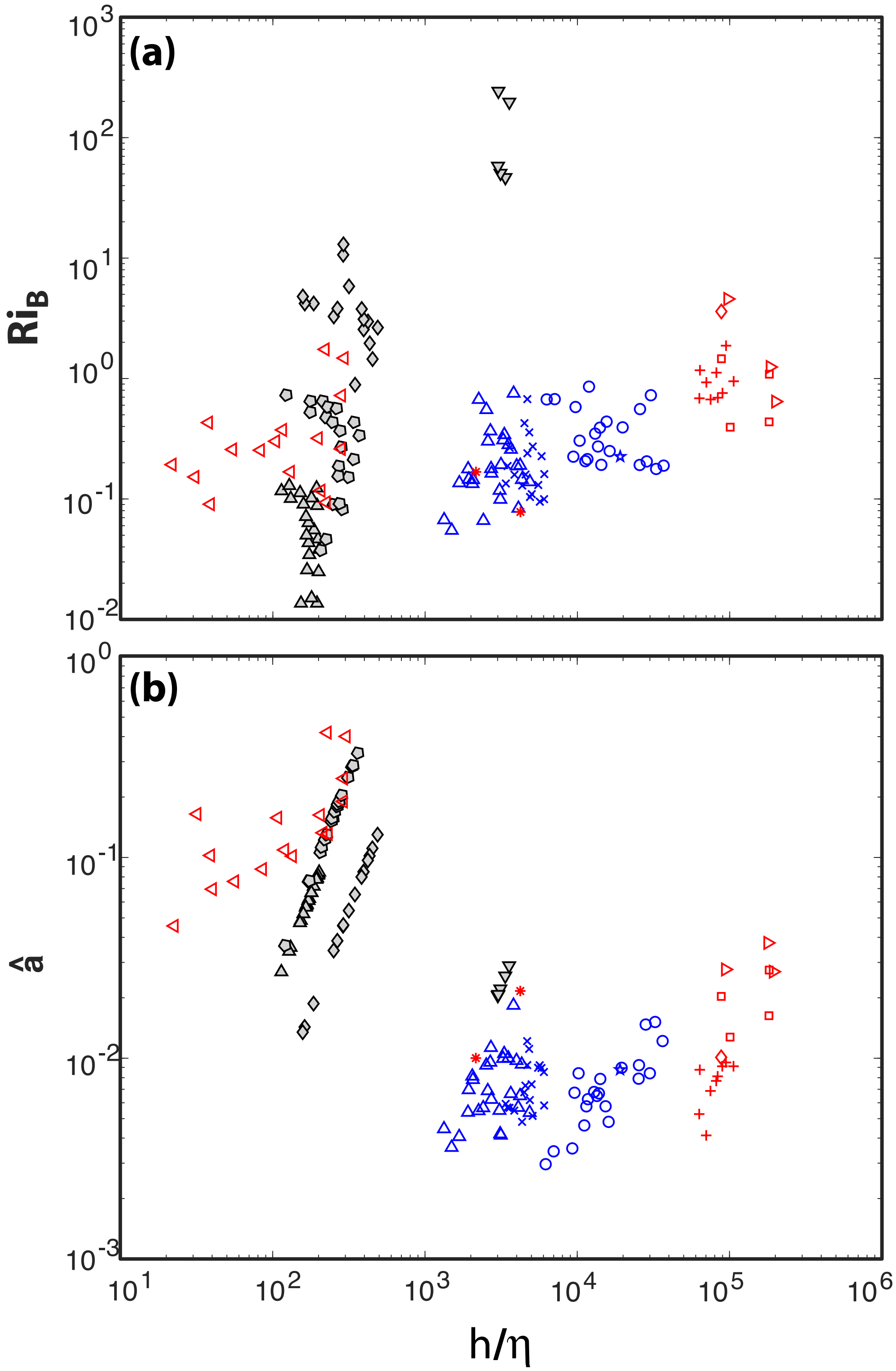


**Figure 5:** (a) Distribution of data in the ***Ri****B* - $\frac{h}{\eta}$ plane, and (b) $\hat{a}$ as a function of $\frac{h}{\eta}$. Note that ***Re*** has been estimated for Legacy data, resulting in the uniformity of these data sets along distinct diagonal lines. Legend as in Figure 3.

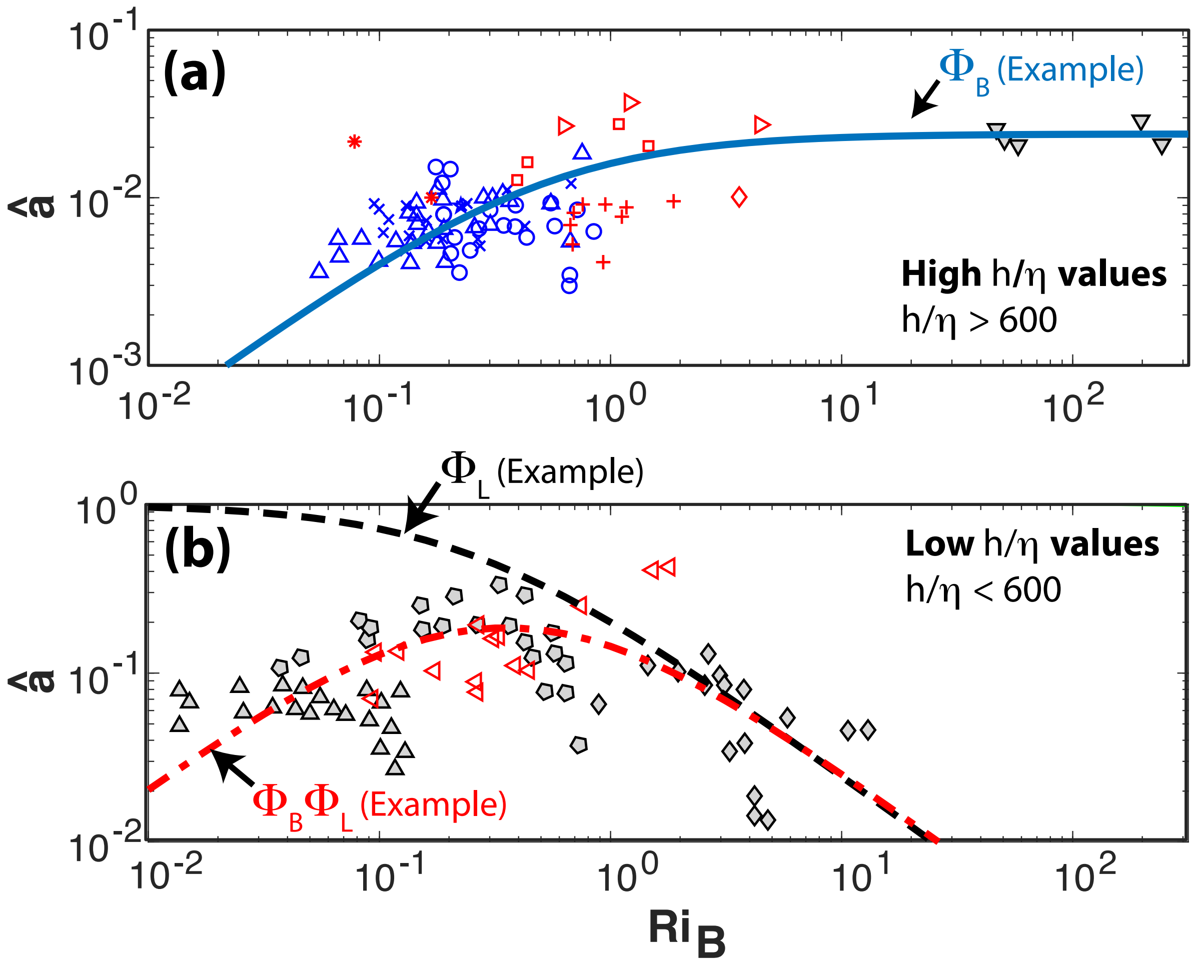


**Figure 6:** $\hat{a}$ as a function of $\boldsymbol{Ri_B}$ for (a) $\frac{h}{\eta} > 600$ (a) and (b) $\frac{h}{\eta} < 600$. Legend as in Figure 3. Example of the general shape of empirical functions $\Phi_B$, $\Phi_L$, and $\Phi_B\Phi_L$ shown by the solid, dashed, and dash-dot lines, respectively.

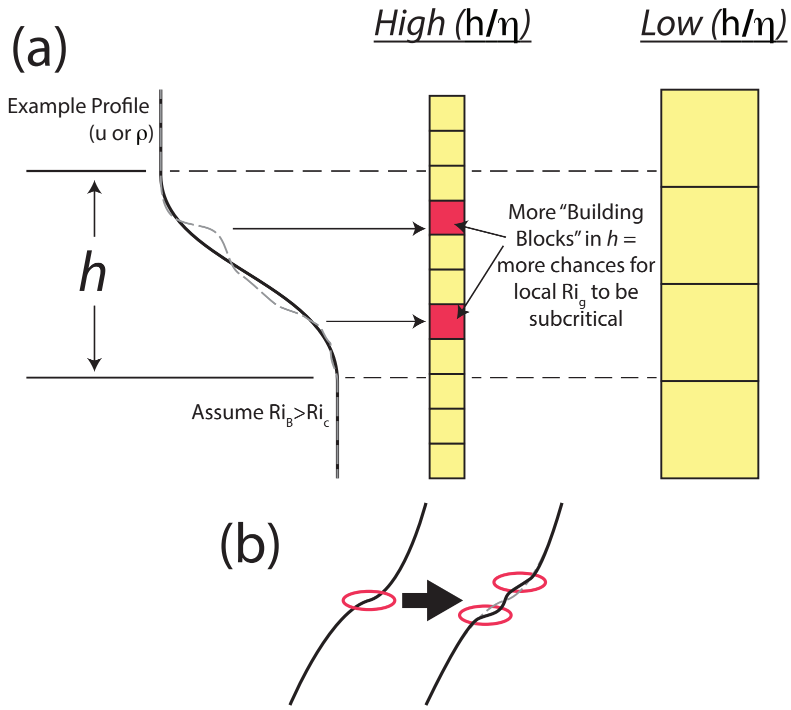


**Figure 7:** (a) Cartoon of "likelihood mechanism". Thicker layers (i.e., higher $\frac{h}{\eta}$ values) offer more opportunities for inconsistencies in the density and velocity profiles to achieve locally subcritical values of $\boldsymbol{Ri_g}$ (as shown by the deviations of the gray dashed profile from the solid profile). Once turbulence is initiated in one "building block", resulting impacts to the local density and velocity profiles will force neighbouring values of $\boldsymbol{Ri_g}$ subcritical and perpetuate the turbulence. (b) Schematic of the spread of turbulence, showing simplified velocity profiles. A critical condition in the profile on the left (identified by the red ellipse) initiates a turbulent event which homogenizes a region in the profile on the right, forcing two new critical conditions due to the compression of existing gradients.

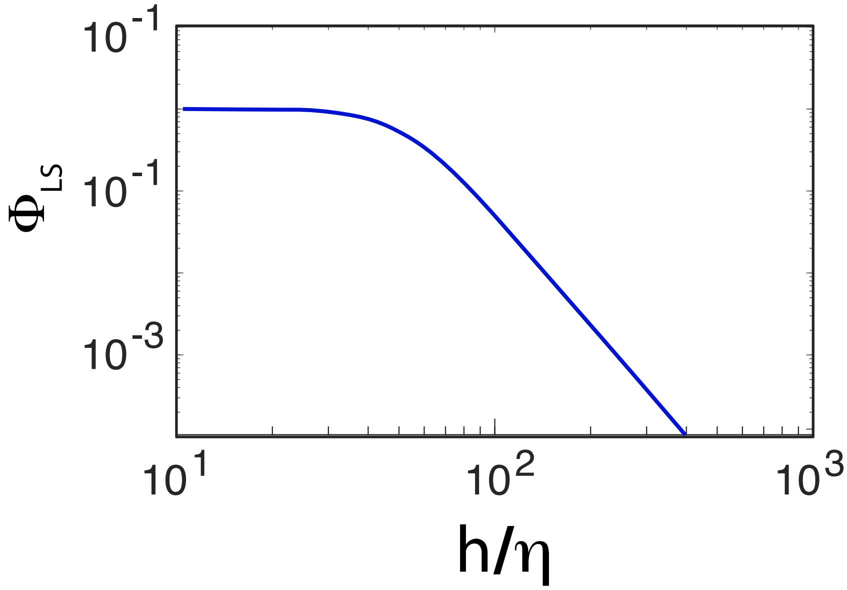


**Figure 8:** Example showing form of $\Phi_{LS}$. Note that value asymptotes to 1 (i.e., $10^0$) for low values of $\frac{h}{\eta}$, ensuring that the roll of point cannot impede beyond the critical $\boldsymbol{Ri_g}$ value.

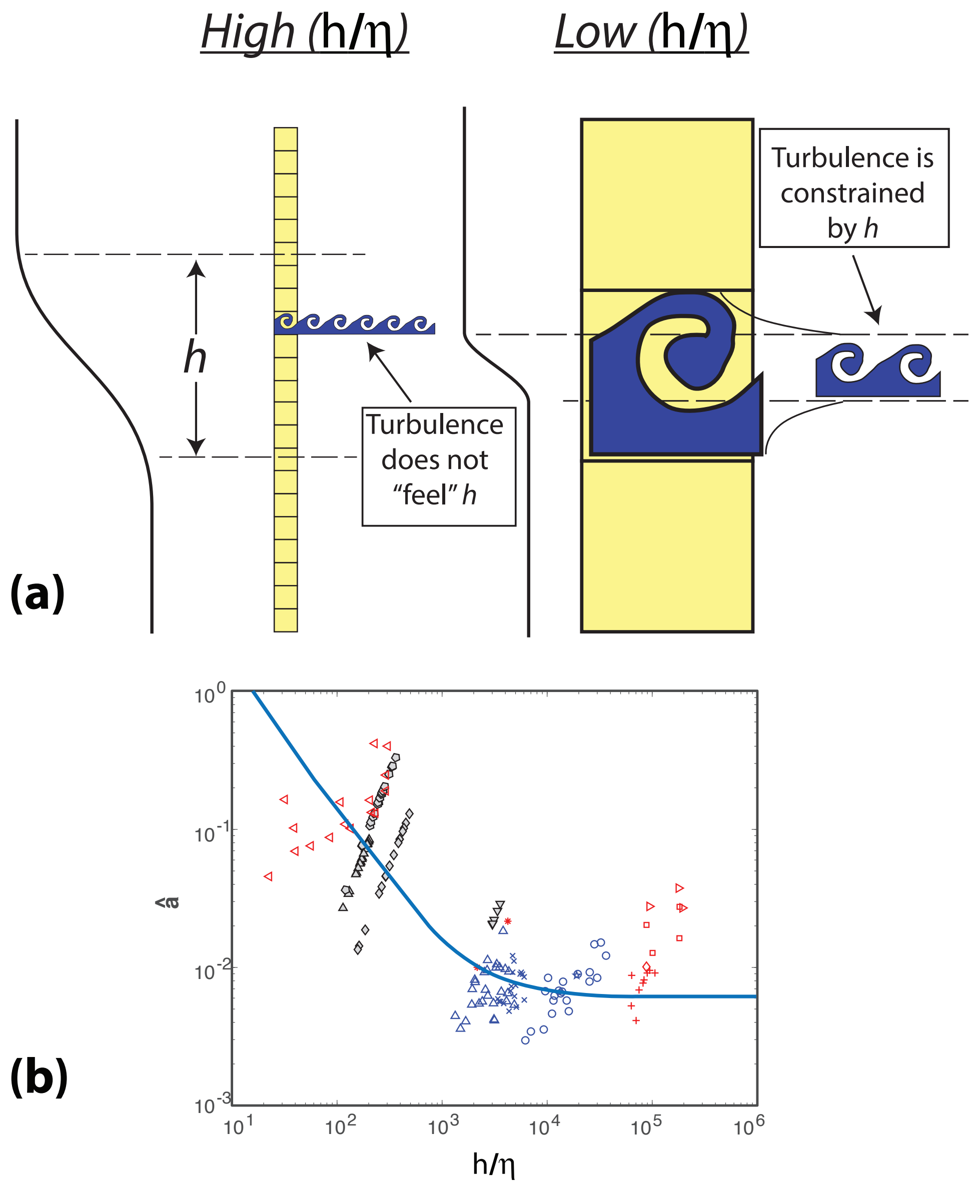


**Figure 9:** (a) Cartoon of energy compression mechanism. Large $\frac{h}{\eta}$ ratios (left) result in turbulent evolution that is not impacted by the layer thickness, h. Small $\frac{h}{\eta}$ ratios (right) result in energy dissipation and mixing primarily within the gradient layer, which may be smaller than the natural KH billow scale. (b) Data from figure 5(b) with example of $\Phi_C$ (solid line) overlaid. Note that $\Phi_C$ is not intended to explain all of the variability in the data but to describe the general trend of the fraction of variability due to the proposed energy compression mechanism.

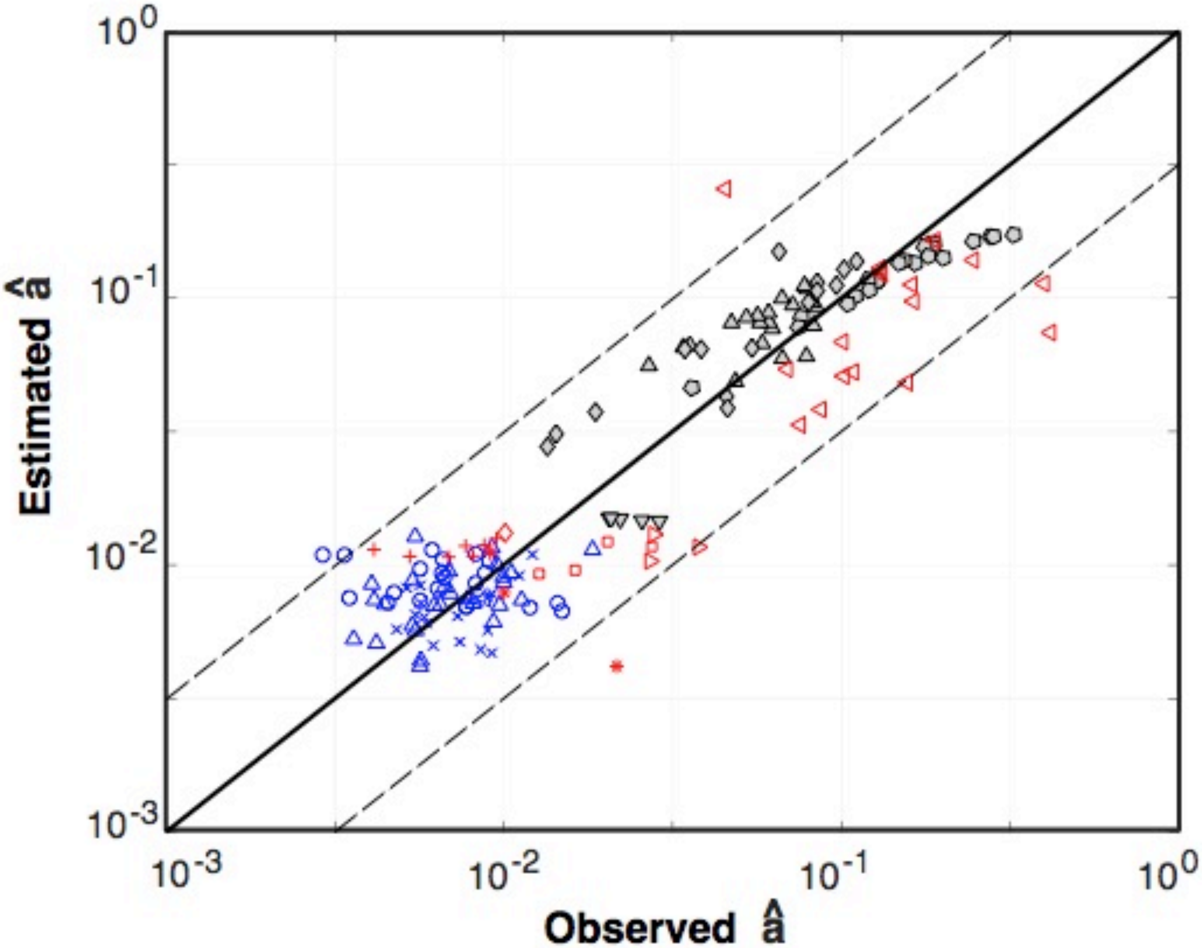


**Figure 10:** Predicted $\hat{a}$ vs. observed $\hat{a}$, using Equation 7, and the coefficients in Table 1. The relationship yields a $\boldsymbol{R^2}$ value of 0.8259. The solid line represents a 1:1 relationship, while the dashed lines are offset by a half order of magnitude to each side. The vast majority of the predicted data falls within the half order of magnitude boundaries. See Figure 3 for data legend.

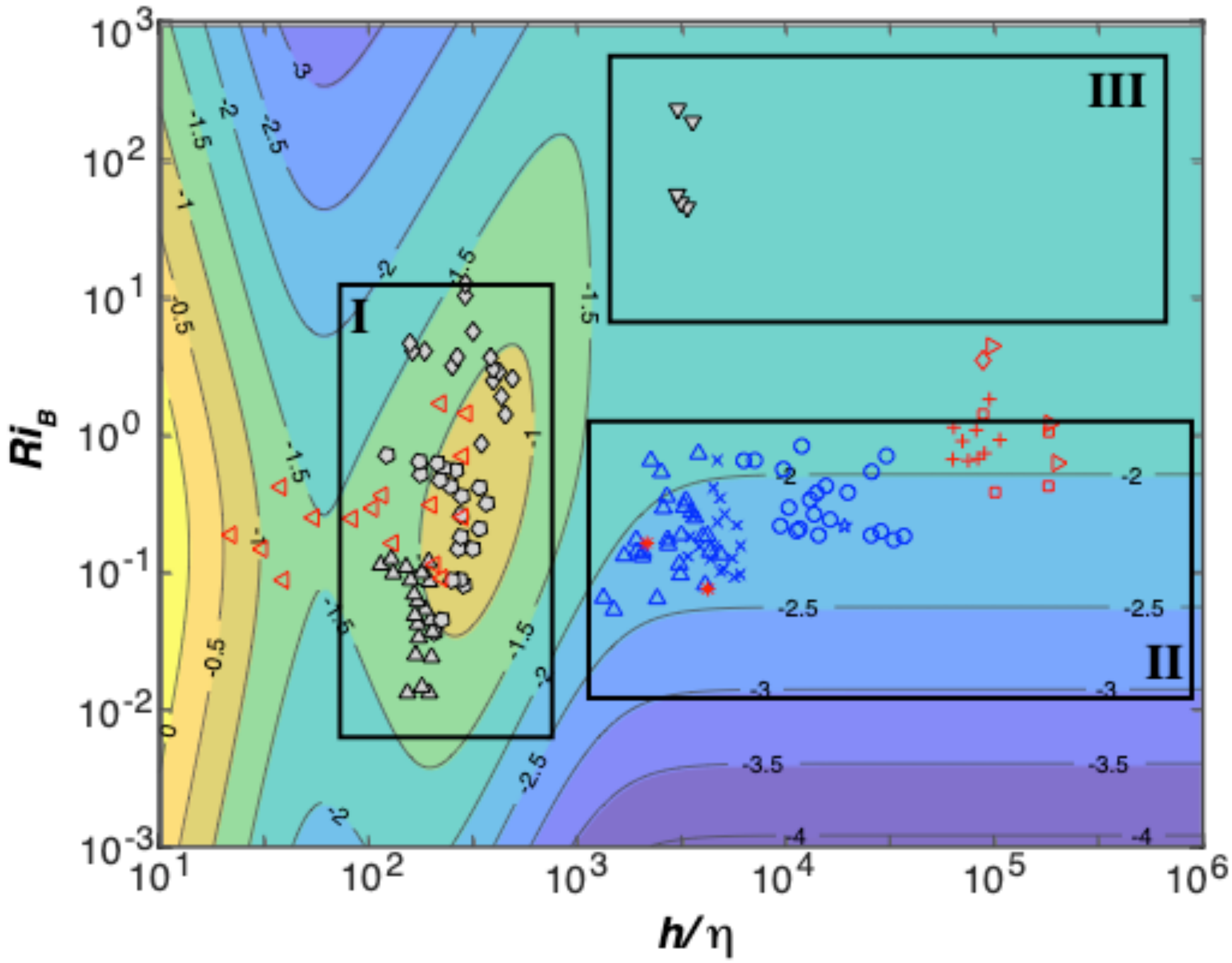


**Figure 11:** Contours of $\hat{a}$ in the $\boldsymbol{Ri_B}$ - $\frac{\boldsymbol{h}}{\boldsymbol{\eta}}$ plane, calculated using Equation 7, and the coefficients in Table 1. Data from Figure 3 is overlain to indicate distribution of data in the $\boldsymbol{Ri_B}$ - $\frac{\boldsymbol{h}}{\boldsymbol{\eta}}$ plane. Rectangular boxes labelled I, II, and III represent specific dynamical regions, as described in the text. See Figure 3 for data legend.

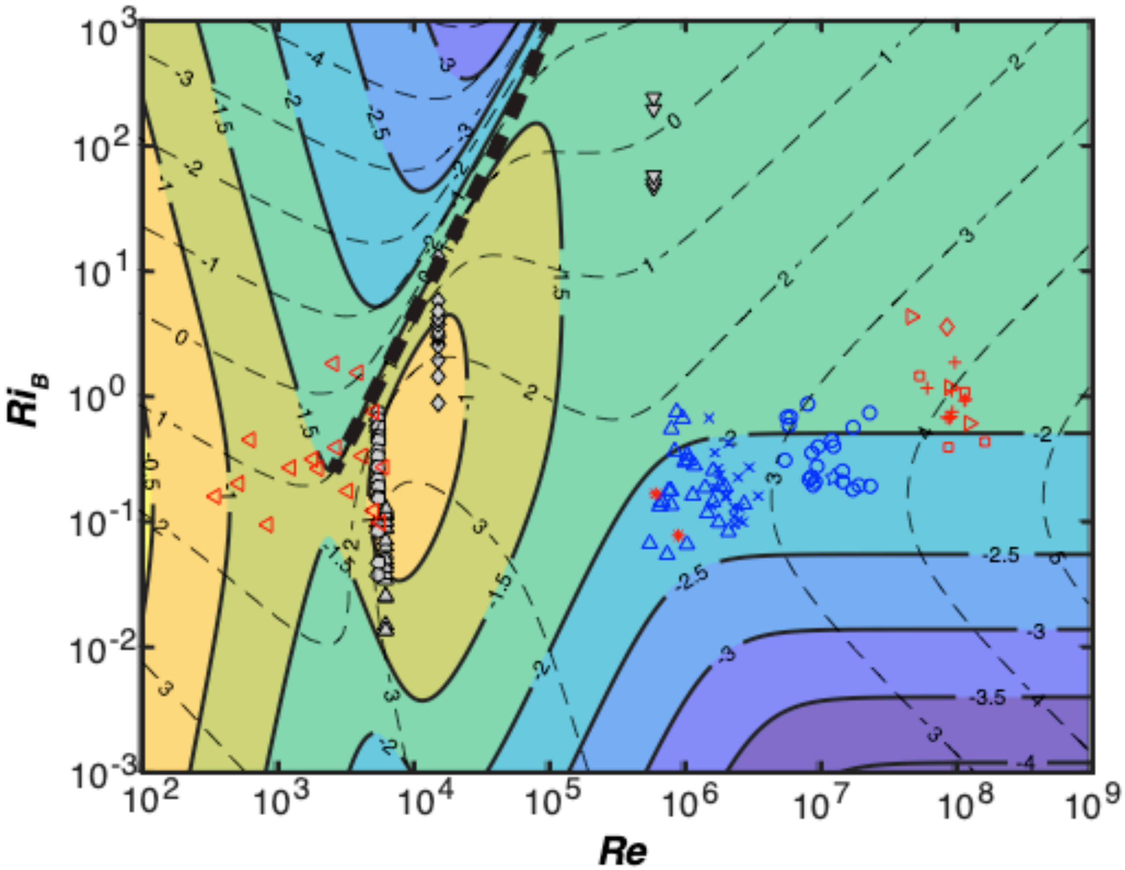


**Figure 12:** Contours of $\hat{\alpha}$ (solid) in the $\boldsymbol{Ri_B}$ - $\boldsymbol{Re}$ plane, calculated using Equation 7, and the coefficients in Table 1. Dashed contours represent the value of $Re_B = \frac{\varepsilon}{\nu N^2}$ (based on bulk flow variables). Data from Figure 3 is overlain to indicate distribution of data in the $\boldsymbol{Ri_B}$-$\boldsymbol{Re}$ plane. The bold dashed black line represents an approximation of "critical" $\boldsymbol{Ri_B}$ value as a function of scale. See Figure 3 for data legend.

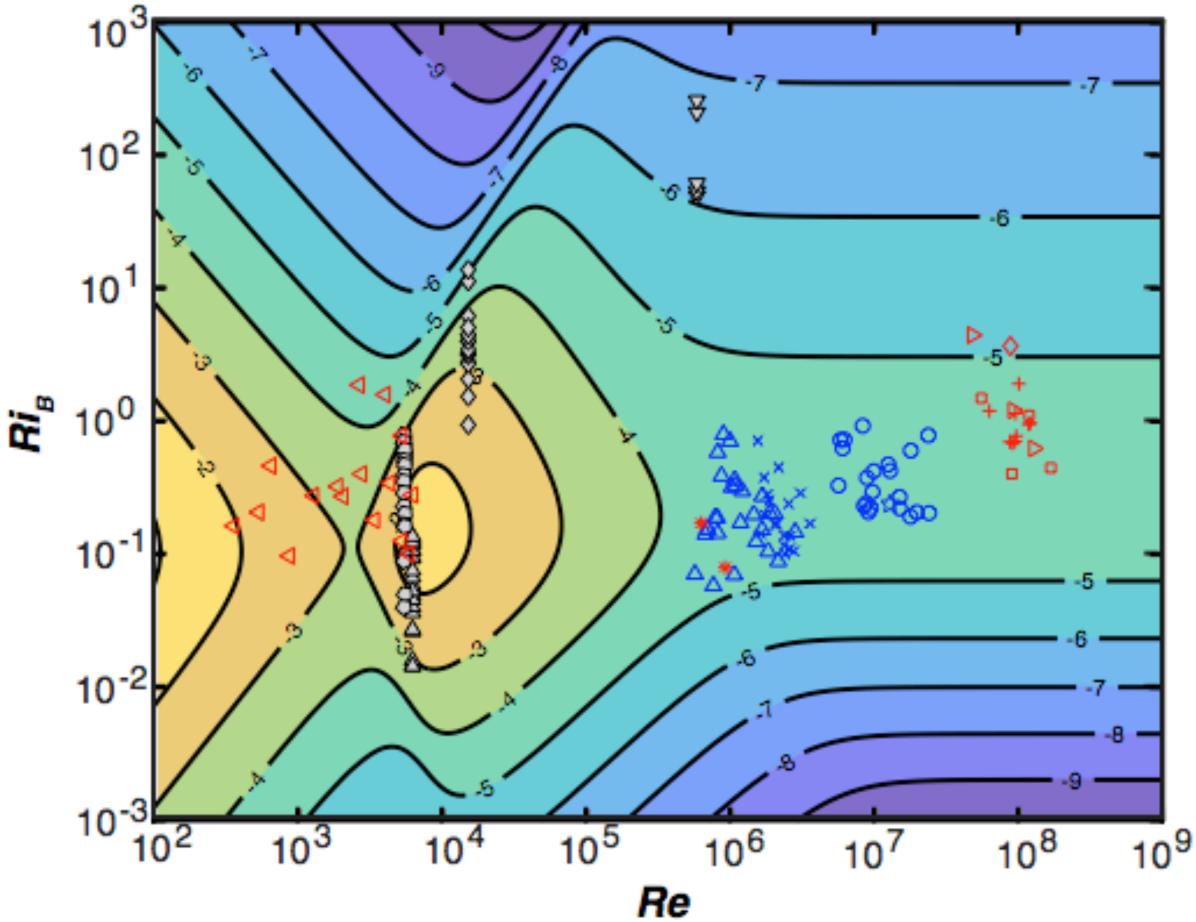


**Figure 13:** Contours of $\xi$ in the $\boldsymbol{Ri_B}$ - $\boldsymbol{Re}$ plane, calculated using Equation 7, and the coefficients in Table 1. Data from Figure 3 is overlain. See Figure 3 for data legend.